

NPS ARCHIVE
1968
TAMNY, M.

TERODYNE
OSPHERIC

50

50F
6328A

968

Thesis
T135

0000
NA
M

002

HETERODYNE MEASUREMENTS OF
ATMOSPHERIC PHASE TURBULENCE AT 6328A

by

Michael Anthony Tamny

B.S., United States Naval Academy

1962

Submitted in Partial Fulfillment of the
Requirements for the Degree of
Naval Engineer and the Degree of
Master of Science in Electrical Engineering
at the
Massachusetts Institute of Technology
May 1968

HETERODYNE MEASUREMENTS OF ATMOSPHERIC
PHASE TURBULENCE AT 6328A

by

MICHAEL ANTHONY TAMNY

Submitted to the Department of Naval Architecture
and Marine Engineering on may 17, 1968 in partial fulfillment
of the requirements for the Master of Science degree in
Electrical Engineering and the Professional Degree,
Naval Engineer

ABSTRACT

This thesis investigates the effects of atmospheric turbulence on the spatial properties of the phase of transmitted beams. Experimental measurements in the form of a series of photographs of interference patterns between two beams were made using a modified optical heterodyne system. The two beams of the heterodyne system were mixed with a very small, controllable angular difference between their directions of approach to the detector. The resulting fringe patterns were affected by the atmosphere as differences between succeeding photographs show. The first order effect of the atmosphere was found to be a tilt relative to the direction of travel. Tilt differences as small as 5 seconds of arc can be measured using this system with assurance; smaller values could be confused with systematic effects.

Thesis Supervisor: Estil V. Hoversten
Title: Assistant Professor of Electrical Engineering



ACKNOWLEDGEMENTS

I would like to express my gratitude to several people who had a part in the development of this thesis. First I would like to thank Professor E. V. Hoversten for his supervision of this thesis. Secondly, I would like to thank the Research Laboratory of Electronics for the generous support this thesis received. Particularly I would like to thank John Moldon of the Research Laboratory of Electronics for his generous assistance in setting up the experiment and his many helpful suggestions.

TABLE OF CONTENTS

page

INTRODUCTION.....	7
TEXT	
CHAPTER 1 - THEORETICAL RESULTS.....	9
1-1 Atmospheric Turbulence.....	9
1-2 Propagation through the Turbulent Atmosphere.....	10
1-3 Received Field Parameters.....	11
1-4 Communication Model.....	12
1-5 Optical Heterodyning.....	13
CHAPTER 2 - EXPERIMENTAL SYSTEM.....	15
2-1 System Layout and Equipment.....	15
2-2 Pattern Detection.....	19
2-3 Experimental System.....	22
2-4 Data Presentation.....	23
CHAPTER 3 - EXPERIMENTAL RESULTS.....	26
3-1 Beam Description.....	26
3-2 Full Aperture Analysis.....	33
3-3 Phase Analysis.....	37
3-4 Narrow Strip Analysis.....	39
CHAPTER 4 - CONCLUSIONS.....	49
4-1 Conclusions.....	49
4-2 Suggestions for Improvement.....	50
APPENDIX A.....	52
APPENDIX B.....	64

FIGURES

1	Optical Heterodyne Geometry.....	14
2	System Layout for Optical Heterodyne.....	16
3	Front View of Downrange Reflector.....	17

4	Rear View of Downrange Reflector.....	18
5	Optical Bench Layout.....	20
6	Optical Bench Layout Showing Local Oscillator Path.....	21
7	Full Aperture Display.....	24
8	Narrow Strip of Aperture Display.....	24
10	Local Oscillator Beam Intensity.....	27
11	Received Beam Intensity.....	27
12	Sequence A Fringe Patterns.....	29
13	Sequence B Fringe Patterns.....	30
14	Sequence C Fringe Patterns.....	31
15	Sequence A Full Aperture Display.....	35
16	Sequence B Full Aperture Display.....	36
17	Sequence C Full Aperture Display.....	36
18	Sequence A Typical Horizontal Lines.....	40
19	Sequence B Typical Horizontal Lines.....	40
20	Sequence C Typical Horizontal Lines.....	40
21	Typical Unaveraged Location of Peak Lines.....	42
22	Sequence A Average Spatial Period.....	43
23	Sequence B Average Spatial Period.....	43
24	Sequence C Average Spatial Period.....	43
25	Sequence A Total Phase Change.....	45
26	Sequence B Total Phase Change.....	46
27	Sequence C Total Phase Change.....	47
A-1	Black Box Model of Detector Surface.....	55
A-2	Data Analysis System Block Diagram.....	59
A-3	Master Clock.....	61

A-4	Eight Counter and Pulse Generator.....	61
A-5	Seven Counter and Pulse Generator.....	62
A-6	Four Counter and Pulse Generator.....	62
A-7	Picture Improvement from Filtering.....	63
B-1	Visibility Ratio vs. Scintillation.....	66

INTRODUCTION

The advent of the laser has stimulated interest in communication at optical frequencies. The potential bandwidths and antenna gains hold great promise, but the degrading effects of the atmosphere on propagating optical wavelength beams have prevented immediate widespread usage. Present efforts in the area of atmospheric optical communication are mainly directed towards gaining an understanding of the atmospheric phenomena and characterizing the received fields after propagation through the atmosphere. This information is necessary to build a statistical model of the channel at optical and near infrared frequencies. A statistical model will allow the use of tools from modern communication theory to establish the ultimate limits of optical communication links utilizing atmospheric channels.

Atmospheric effects on propagated fields at optical and near infrared frequencies can be broadly put into three categories:

1. Molecular absorption
2. Particle scattering
3. Turbulence

The first two are more or less suggestive and under some conditions these two effects can be lumped as a path-length dependent loss term. This assumption depends strongly on atmospheric conditions and propagating wavelengths. However, with a clear atmosphere this model is reasonable at a wavelength of 6328\AA . This thesis deals with the third effect, turbulence.

Turbulence is the name used to describe the effects of small variations in the local refractive index caused by turbulent mixing of the atmosphere under wind and temperature gradients. At-

mospheric turbulence results in an inhomogeneous medium, and propagation through this medium causes random spatial and temporal fluctuations in amplitude and phase of the received field. A body of work has been done on the amplitude fluctuations, called scintillation, with beams. There has been less emphasis on the phase process due to the difficulty of phase measurements.

This thesis considers a method of phase measurement using an optical heterodyne system and evaluation of the experimental measurements.

Chapter 1 presents a brief survey of the pertinent theory and modeling necessary for this thesis.

Chapter 2 describes the experimental system used to heterodyne at 6328\AA and the data analysis system in general. Appendix A contains a more detailed explanation of the system, special devices, and electronic circuits.

Chapter 3 presents the experimental results. Appendix B contains more detailed information on the method of data extraction.

Chapter 4 considers the experimental results and conclusions.

CHAPTER 1

This chapter is concerned with some of the theoretical results developed for beam propagation through the turbulent atmosphere with emphasis on those results pertinent to the experimental system constructed.

1 - 1 Atmospheric Turbulence

The effects of atmospheric turbulence on optical wavelengths have long been known to astronomers; the twinkling of starlight on a windy night is a common example. The possible use of the laser for atmospheric communication links has renewed interest in the study of atmospheric turbulence and its effects.

Turbulence is small scale variations of the index of refraction, typically on the order of 1 part in 10^6 , caused by temperature discontinuities set up by turbulent mixing of the atmosphere. These refractive index changes were first described using a Gaussian correlation function which was an analytically convenient method but led to questionable results. A second path taken by Tatarski applied the Kolmogorov theory of turbulent flow at very large Reynolds numbers to the index variations.¹ This analysis leads to a second moment description of the medium, a method that is not alone sufficient to describe atmospheric turbulence. However, the fields propagated through the inhomogeneous medium will have lognormal statistics; thus a second moment description of the medium will be adequate to handle the received field statistics. The results of Tatarski's work show that the turbulence is locally isotropic and homogeneous and has a structure function of the form¹

$$D_n(\rho, \bar{R}) = \begin{cases} c_n^2(\bar{R}) \rho^{2/3} & \ell_0 \ll \rho \ll L_0 \\ c_n^2(R) \ell_0^{2/3} \left(\frac{\rho}{\ell_0}\right)^2 & \rho \ll \ell_0 \end{cases} \quad (1)$$

where

$$D_n(\rho, \bar{R}) = [n(\bar{r}_1) - n(\bar{r}_1 + \rho)]^2 \quad (2)$$

$$\bar{R} = \frac{2\bar{r}_1 + \bar{\rho}}{2} \quad \text{where } \bar{R} \text{ is a vector. A bar will be used to denote vectors.}$$

$$\rho = \bar{\rho}$$

$$c_n^2(\bar{R}) = \text{constant associated with the magnitude of the turbulence at } \bar{R}$$

$$n(\bar{r}) = \text{refractive index at } \bar{r}$$

$$\ell_0 = \text{inner scale of turbulence; on the order of 1mm and related to the breakup of laminar flow. At distances greater than } \ell_0, n(\bar{r}) \text{ tends to be discontinuous.}$$

$$L_0 = \text{outer scale of turbulence; on the order of meters and related to the gross layer structure of the atmosphere or the distance between obstacles.}$$

The model, while not as convenient analytically, is generally considered better than the Gaussian correlation function/^{description} and has been the basis for most further work.

1 - 2 Propagation through the turbulent atmosphere

The available theoretical solutions generally are for infinite plane wave sources and assume a "frozen" atmosphere, where the turbulence is fixed in space. The frozen-in structure is assumed to move across the transmission path due to the component of wind normal to the propagation path to account for the temporal behavior. The three basic approaches to the turbulent propagation problem are:
 1
 using a Rytov approximation to the wave equation, solving the wave

equation for the mutual coherence function,² and a geometric optics type of solution.³ The last method, geometrical optics, is generally considered inferior since it does not account for diffraction effects on long paths with small scale inhomogeneities.

1 - 3 Received Field Parameters

Using the "frozen" atmosphere assumption, the central limit theorem, and one of the solution approaches, it can be shown that a time sample of the received field envelope is a lognormal random variable, and that a time sample of the received field phase is a Gaussian random variable. There is evidence to expect that the form of these statistics is unchanged for beam propagation.

Another measure of importance is the spatial coherence of the phase of the received field. Tatarski has derived an expression for the case of a linearly polarized plane wave with the atmospheric turbulence described as in Eq. 1, and $C_n^2(\bar{R})$ a constant independent of \bar{R} .¹ Then

$$D_\phi(\bar{\rho}) = \alpha C_n^2 k^2 L \rho^{5/3} \quad (3)$$

where $D_\phi(\bar{\rho})$ is the phase structure function, k the wave number of the radiation, L the path length, and

$$\alpha = \begin{cases} 2.91 & \rho > \lambda L \\ 1.45 & \ell_0 \ll \rho \ll \lambda L \end{cases}$$

Using the expression for $D_\phi(\bar{\rho})$ in Eq. 3, a coherence diameter for some selected mean-square difference in phase can be calculated.

One example quoted in Hoversten from Goldstein⁹ is

$$D_{\text{coherent}} = 1.75 \times 10^{-2} \frac{\lambda^2}{C_n^2 L} \quad (4)$$

Fried has used a form of Eq. 3 to show that wave front tilting is the largest contributor to distortion.⁵

Another parameter is the frequency spectrum of the amplitude and phase turbulence processes. Measurements of intensity spectrums have shown them to be no more than several hundred cycles wide for most conditions.^{6,7} Measurements for the phase process are not as plentiful, but recent measurements have shown that the spectrum is no more than several hundred cycles wide.⁸

1 - 4 Communication Model

A suggested model describing the effects of the turbulent atmosphere as a communication channel, when particle scattering is not important, is a multiplicative channel with additive background noise.⁹ A linearly polarized field (chosen for simplicity) in the absence of losses, turbulence and background noise would be received as

$$E_{\text{rec}}(\vec{r}, t) = \text{Real} \left\{ \underline{E}(\vec{r}, t) e^{j\omega t} \right\} \quad (5)$$

When turbulence and background noise are present the received field (again in the absence of losses) would be

$$E_{\text{rec}}(\vec{r}, t) = \text{Real} \left\{ \underline{E}(\vec{r}, t) e^{j\omega t} \delta(\vec{r}, t) + \underline{E}_n(\vec{r}, t) e^{j\omega t} \Theta(\vec{r}, t) \right\} \quad (6)$$

where

$e^{\delta(\vec{r}, t)}$ represents the effect of the turbulent channel

$$\delta(\vec{r}, t) = X(\vec{r}, t) + j\phi(\vec{r}, t)$$

$X(\vec{r}, t)$ represents the scintillation process

$\phi(\vec{r}, t)$ represents the phase distortion process

$E_n(\vec{r}, t)e^{j\Theta_n(\vec{r}, t)}$ represents the relevant polarization component of the background radiation; a complex Gaussian process with a very wide bandwidth on both E_n and Θ_n .

1 - 5 Optical Heterodyning

Two waves simultaneously incident on a surface will cause an interference pattern. This can be modeled simply, using plane waves of the same frequency and linear polarization. When the two waves

beat together from slightly different directions, $\vec{\beta}_1$ and $\vec{\beta}_2$, a fringe pattern whose period is related to the difference in approach angle is created. If one of the waves has been sent through the atmosphere, it will have a phase term proportional to the phase distortion process. Thus if complex notation is used, suppressing the $e^{j\omega t}$ time variations for simplicity, the fields can be described as (see Fig. 1)

$$E_{rec}(\vec{r}, t) = E_1 e^{-j\beta_z z} X(\vec{r}, t) e^{j\phi(\vec{r}, t)} \quad (8)$$

$$E_{Lo}(\vec{r}, t) = E_2 e^{-j\beta_z z - j\beta_x x} \quad (9)$$

where

$$|\vec{\beta}_1| = |\vec{\beta}_2| = \sqrt{\beta_z^2 + \beta_x^2} = \frac{\omega}{c} = \frac{2\pi}{\lambda} \quad \text{and } \vec{\beta}_1 \text{ and } \vec{\beta}_2 \text{ are wave vectors.}$$

Then on the surface ($z=0$) shown in Fig. 1 the total field can be written as

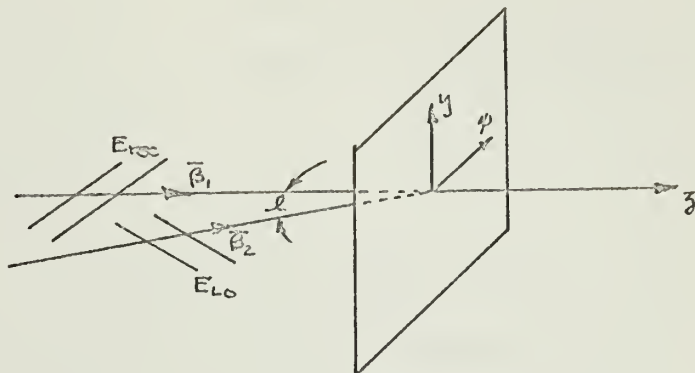
$$\begin{aligned} E_{total}(\vec{r}, t) &= E_{rec}(\vec{r}, t) + E_{Lo}(\vec{r}, t) \\ &= E_1 e^{X(\vec{r}, t)} e^{j\phi(\vec{r}, t)} + E_2 e^{-j\beta_x x} \end{aligned} \quad (10)$$

where

$$\vec{\rho} = \vec{i}_x x + \vec{i}_y y$$

$$\vec{r} = \vec{\rho} + \vec{i}_z z$$

Figure 1.
Optical Heterodyne
Geometry



Then the intensity on the surface is

$$\begin{aligned} I(\vec{\rho}, t) &= \frac{1}{2\eta} \left\{ \underline{E}_{\text{total}} \underline{E}_{\text{total}}^* \right\} \\ &= \frac{1}{2\eta} \left\{ |\underline{E}_1|^2 e^{2X(\vec{\rho}, t)} + |\underline{E}_2|^2 + 2 |\underline{E}_1| |\underline{E}_2| e^{X(\vec{\rho}, t)} \cos[\beta_x x - \phi(\vec{\rho}, t) - \alpha] \right\} \end{aligned} \quad (11)$$

where η is the impedance of the atmosphere and α represents the phase angle between the complex amplitudes \underline{E}_1 and \underline{E}_2 . Thus a portion of the intensity is a term phase modulated by the atmospheric phase distortion. In the experimental section of this thesis a system to exploit this effect is described in detail.

CHAPTER 2

This chapter describes the system developed to create a spatial interference pattern between two beams of coherent light, one modulated by atmospheric turbulence.

2 - 1 System Layout and Equipment

The basic arrangement for heterodyning is shown in Fig. 2. The source was a Spectra-Physics Model 119 Helium-Neon gas laser operating at a wavelength of 6328\AA . The Model 119 laser has a rated continuous output power of 0.1 milliwatt although measurements indicated slightly higher values during experimentation. The beam from one end was collimated using a Spectra-Physics Model 331-333 spatial filter-collimator and transmitted over an atmospheric path. The down range reflector, shown in Fig. 3 and Fig. 4, is a sixteen-inch diameter flat mirror mounted in an aluminum collar and frame. The collar and frame have precision adjustments through screw-arm systems that allow very accurate pointing of the return beam. The beam from the opposite end of the laser was reflected off two flat first surface mirrors mounted on precision adjustment holders to reach the combining beam splitter. No lens was used in this non-atmospheric path to minimize extraneous lens aberrations. As this beam was close to plane wave conditions by the time it reached the combining beam splitter, its curvature was easily matched by the telescope output using the telescope eyepiece.

The receiving telescope is a three-inch reflector with an eighteen-inch focal length. The lens from a Praktica FX-3 camera ($f/2.8$, 50 millimeter focal length) was used as the eyepiece for

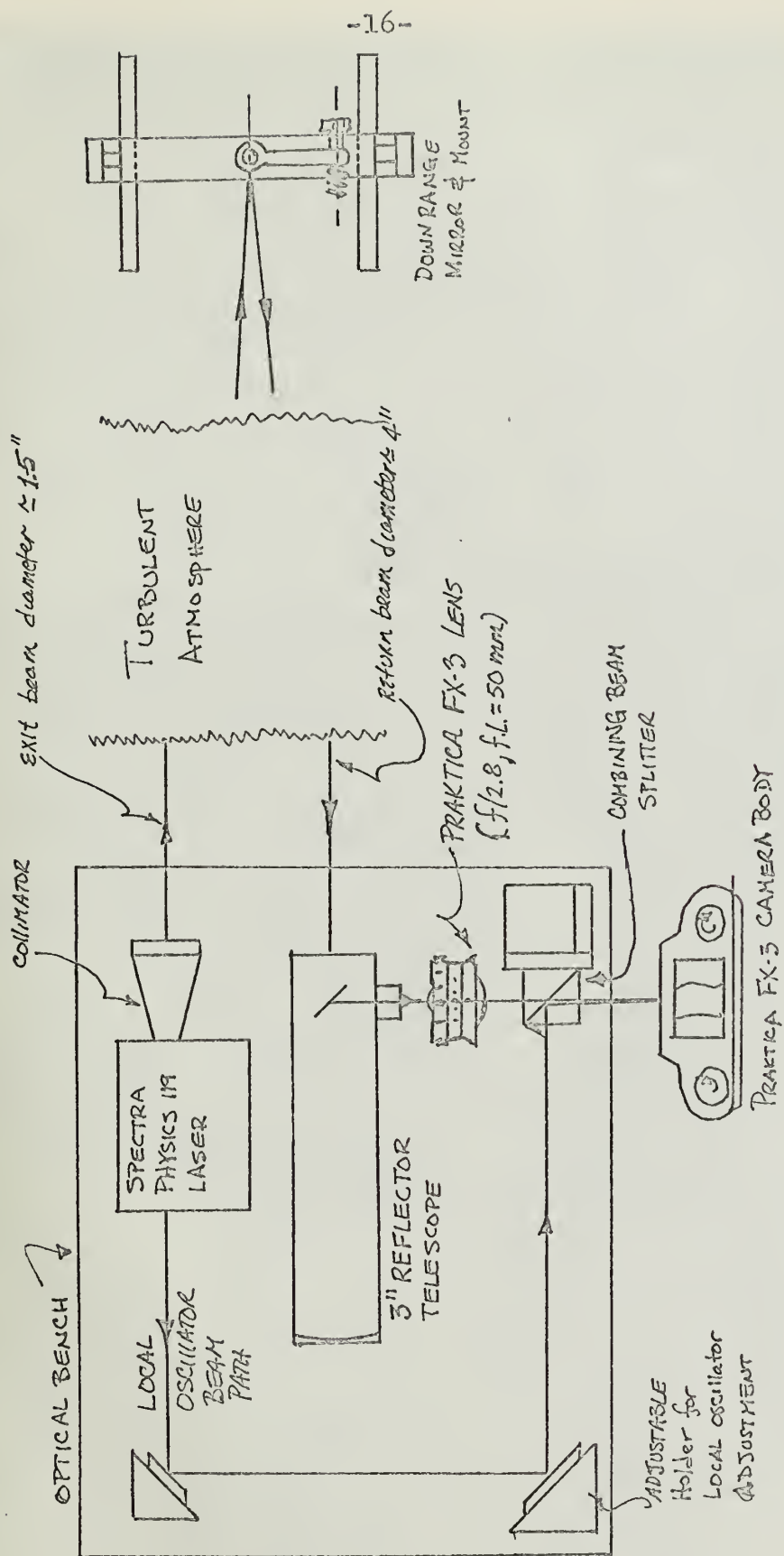


Figure 2. System Layout for Optical Heterodyne



Figure 3. Front View of Downrange Reflector and Mount



Figure 4. Rear View of Downrange Reflector and Mount

several reasons; the 50 millimeter focal length meant the telescope output beam size closely matched the local oscillator beam size and the focusing ring of the eyepiece allowed adjustments to be made with a minimum of mechanical movement.

The two signals were combined using a fifteen-millimeter prismatic beam splitter mounted on a fine adjustment holder. This mount was used to manipulate the fringe spacing and orientation since relatively small changes in angular separation can be made most easily at this point.

All of this equipment, with the exception of the large downrange reflector, was bolted down on a two-inch thick aluminum optical bench housed in a penthouse on the roof of Building 20 at M.I.T. (See Figs. 5 and 6). The downrange reflector was housed in a protective box on the other end of the roof of Building 20, making the atmospheric path approximately 200 meters round trip.

2 - 2 Pattern Detection

The interference pattern of the two beams was recorded on black and white film using a Praktica FX-3 35mm single lens reflex camera. The 35mm negatives were developed using Kodak formula D-76 developer, standard for the Tri-X film used, and were mounted in holders to be used as slides for later projection. The negatives were used directly for this projection step since the pattern of light and dark fringes was the same whether or not the image intensities had been reversed.

The fringe patterns were examined in detail using a slide projector to put the image on a screen. This image was then scanned using a Packard Bell Model 920 television camera. The



Figure 5. Optical Bench Layout Showing Laser/Collimator, Receiving Telescope and Eyepiece, Combining Beam Splitter, and Camera

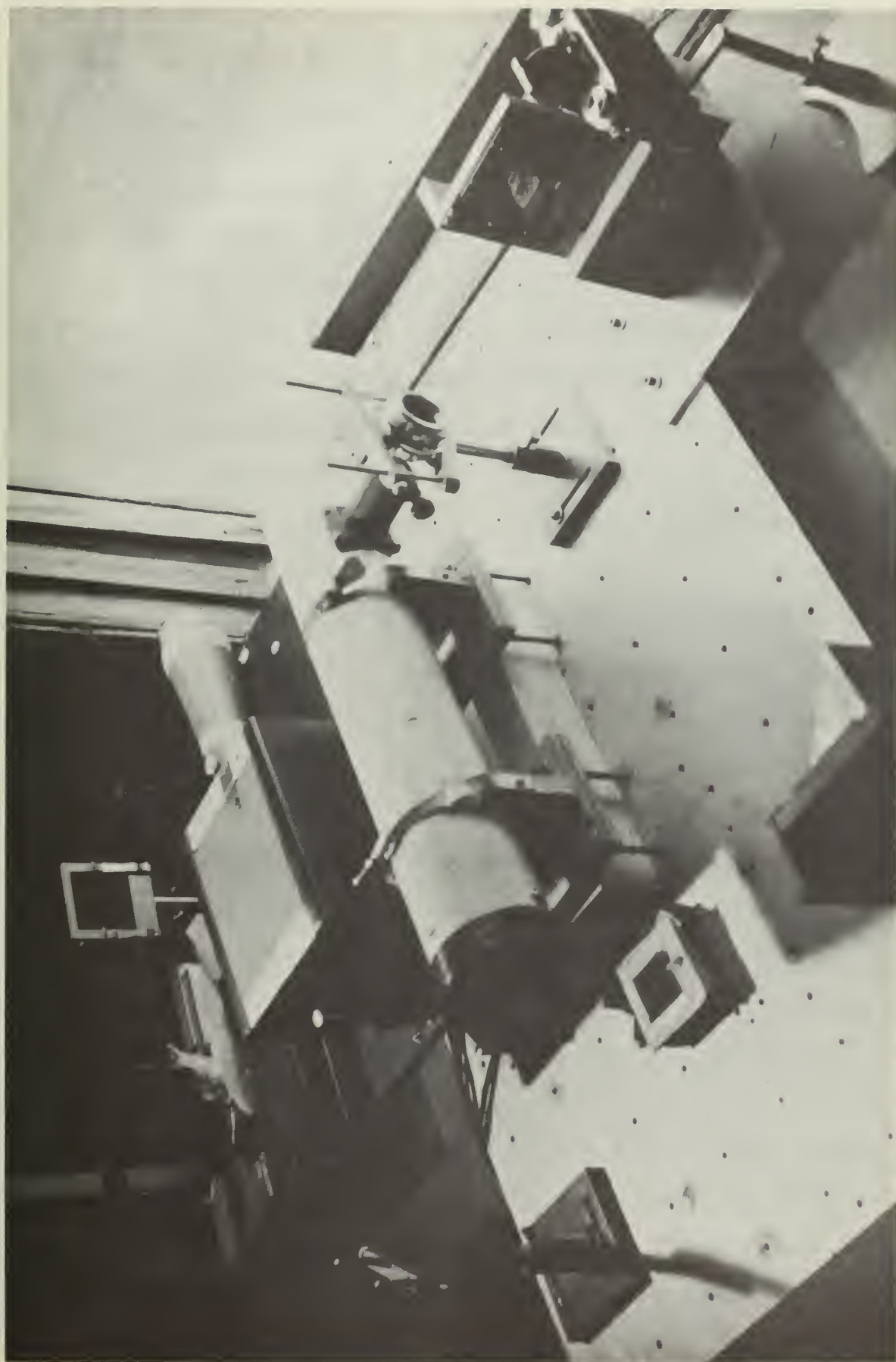


Figure 6. Optical Bench Showing Local Oscillator Path

video output of the television camera was displayed on a Tech-tronix Model 545 oscilloscope as described in section 2-4.

2 - 3 Experimental Procedure

The alignment between the source and receiver was accomplished by finding the laser (not turned on) image in the receiving telescope and down-range mirror system during daylight hours. Thus the optical axis between laser, mirror, and telescope was established. The laser beam could by angular adjustment of the laser mount then be put on the mirror at night to have this beam direction coincide with the optical axis.

At this point the beam emerging from the opposite end of the laser was positioned with the small flat mirrors so that it pointed at the center of the beam splitter. All further adjustments were made using the beam splitter. The local oscillator signal, making a right angle change in direction was much more sensitive to the movement of the beam splitter than the beam coming out of the telescope going straight through. Thus the local oscillator beam could be moved without disturbing the telescope output.

The beams coming out of the beam splitter could be safely observed by eye after they had passed through a Kodak#2 Wratten filter. Without an eyepiece the beams appeared as pencil points which could be adjusted to coincide. An eyepiece could then be used to see the resulting fringe pattern.

After establishing a fringe pattern, the filter was removed and the Praktica FX-3 camera without lens was used to record sequences of three to six consecutive frames of the same fringe pattern i.e., three to six frames were exposed without altering the optical system.

2 - 4 Data Presentation

The slides used for analysis were scanned using a Packard Bell 920 television camera synchronized to an external clock. This same clock output was used to trigger the oscilloscope.

The video output was displayed in two distinctive manners. The first method was designed to obtain an overall picture of the fringe process across the aperture, the second method to look at narrow strips of the fringe process across the aperture.

The first method is shown in block diagram form in Figure 7. The horizontal sweep lines, modulated by the alternating dark and light strips of the projected fringe patterns, were displayed one on top of the other by setting the time base of the oscilloscope to the horizontal sweep time of the television camera. The vertical deflections of each line represent the tones of grey as scanned. Then a ramp signal was added to the horizontal sweep lines to separate them out vertically. This ramp signal was synched to the vertical sweep time of the television camera. Thus a quasi-television picture is made with vertical voltage deflections replacing shades of grey.

The second method used to display the television scan was to select out one individual horizontal scan line with the system as shown in Figure 8. The "A|clock delayed by B clock" mode of the Techtronix 545 oscilloscope was used. The A delayed by B mode is a system where first a ramp signal set to the B clock time base is generated. This ramp signal is compared to a value dialed in by the scope operator. When the two signals are equal, the A clock is armed to take the next trigger it sees and, when triggered, to

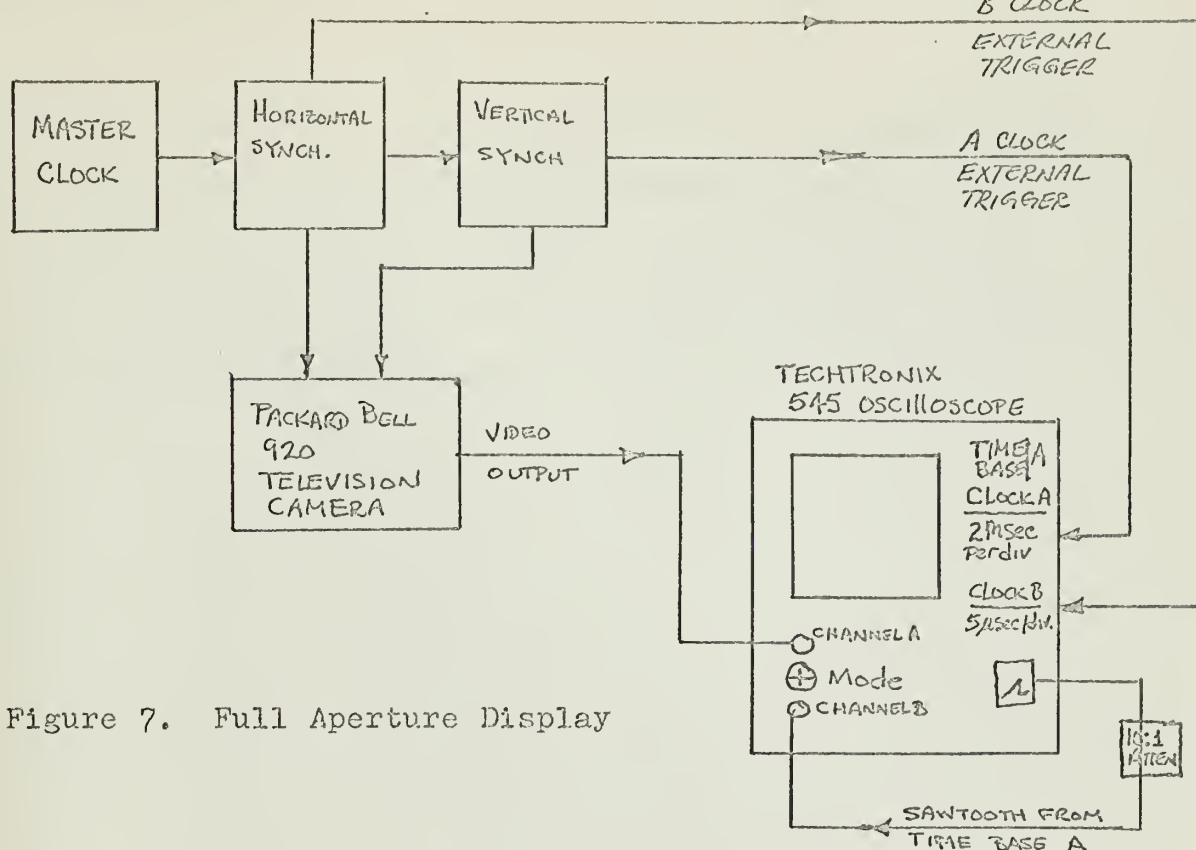


Figure 7. Full Aperture Display

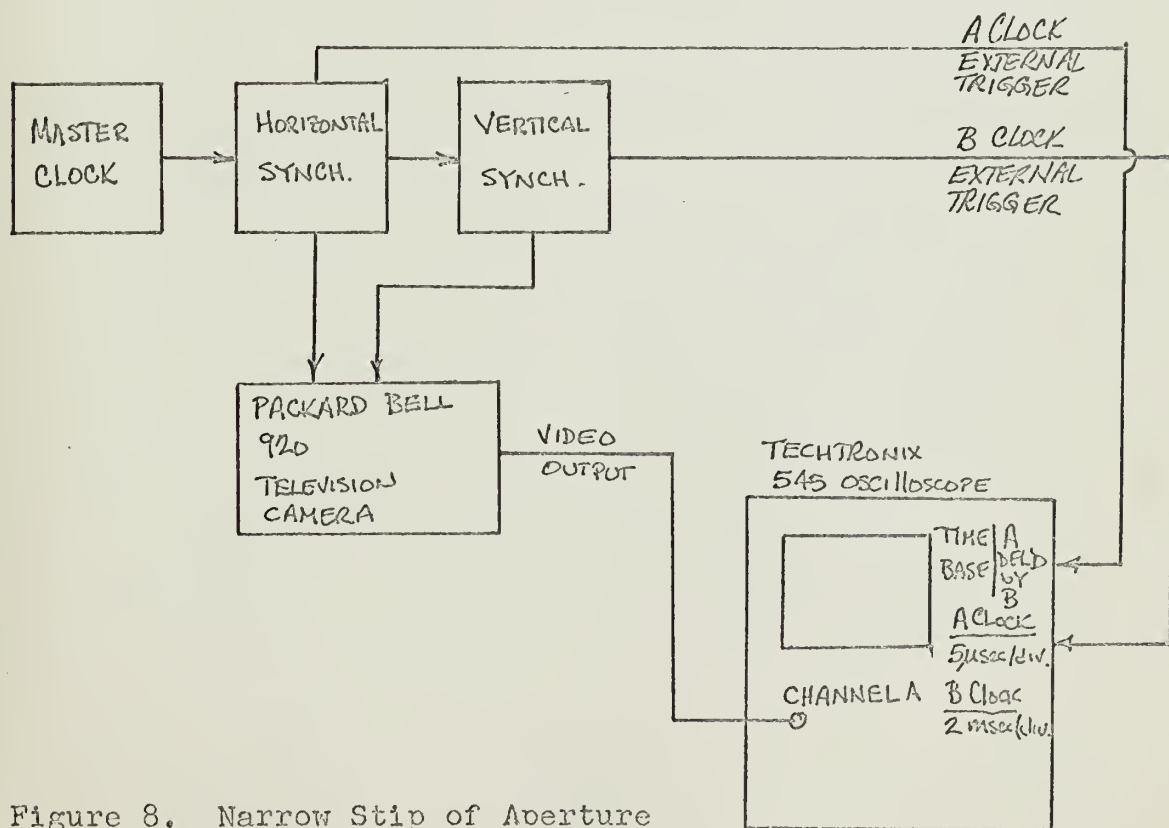


Figure 8. Narrow Strip of Aperture Display

sweep once on its time base. Thus one sweep (A) in a sequence (B) can be selected. By having the B clock synched to the vertical sweep of the television camera and displaying with the A clock . . synched to the horizontal sweep of the television camera, a select- ed horizontal sweep of the television camera can be displayed.

CHAPTER 3

Chapter 3 describes the experimentally observed results and the descriptions of the phase processes inferred from this data.

3 - 1 Beam Description

The individual intensities of the local oscillator beam and the transmitted beam after propagation through the atmosphere and receiver optics are shown in Figures 10 and 11 respectively. These photographs were made by simply blanking off the other beam, and so represent typical intensity distributions at the film surface for each of them. The picture of the intensity over the receiver aperture shows the effects of scintillation, ie., a non-uniform distribution of intensity with a spatially random pattern. The blank spot in the middle and the strip running off to the right in Figure 11 are due to the secondary mirror of the Newtonian telescope used as the receiver. Although this mirror blanks off an appreciable portion of the photograph, enough of the aperture is seen to allow analysis.

When the two beams are present simultaneously and allowed to interfere on the film surface, the fringe patterns shown in Figures 12, 13 and 14 are created. It was found through experimentation that easily discernable changes in the fringe spacing over the aperture could not be seen unless the number of fringes was reduced to approximately twenty or less. If the model of Appendix A is assumed, then equation (A-12) describes the fringe pattern as

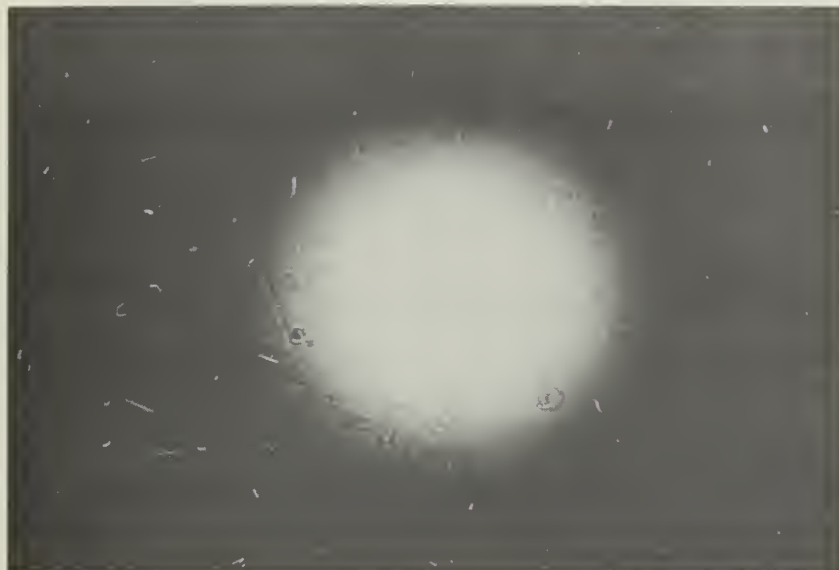


Figure 10. Local Oscillator Beam Intensity at Detector Surface

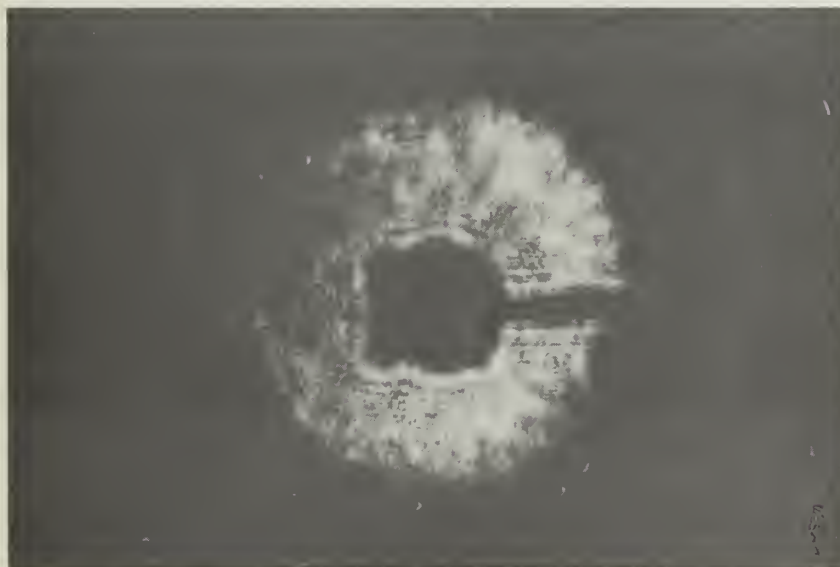


Figure 11. Transmitted Beam Intensity at Detector Surface after traversing Atmospheric Path and Receiving Optics.

$$I(\vec{\rho}) = \frac{1}{2\eta} \left\{ \left| \underline{U}_2 \right|^2 + N^2 + \mu^2 L^2 \left| \underline{U}_1 \right|^2 e^{2X(\vec{\rho})} + 2\mu L \left| \underline{U}_1 \right| \left| \underline{U}_2 \right| e^{X(\vec{\rho})} \cos[\vec{B}_\rho \cdot \vec{\rho} - \phi(\vec{\rho}) - \alpha] \right\} \quad (A-12)$$

where

\underline{U}_1 represents the amplitude of the envelope of the field sent through the atmosphere

\underline{U}_2 represents the amplitude of the envelope of the local oscillator field where α is the phase angle between \underline{E}_1 and \underline{E}_2

N represents the average collected background radiation intensity

L represents the losses in sending a beam through the atmospheric channel and in collection

\vec{B}_ρ represents the direction cosine between the two waves at the detector surface (see Fig. 1)

η represents the impedance of the atmosphere

μ represents the magnification of the telescope and eye-piece

$e^{X(\vec{\rho})}$ represents the scintillation process due to turbulence

$\phi(\vec{\rho})$ represents the phase distortion process due to turbulence

This intensity expression reflects the fact that this pattern is assumed to be a time sample of the fields. It contains only spatially varying terms and implicitly assumes that this pattern is taken for a particular time t . At some later time a photograph would have another time evolution of the sample functions $X(\vec{\rho})$ and $\phi(\vec{\rho})$.

As shown in Appendix B, the geometry can be selected so that the fringes occur along one of the axes in the $\vec{\rho}$ plane. With this geometry the direction cosine, \vec{B}_ρ , can be related to the difference in approach angles, ℓ , of the two beams so that the intensity be-

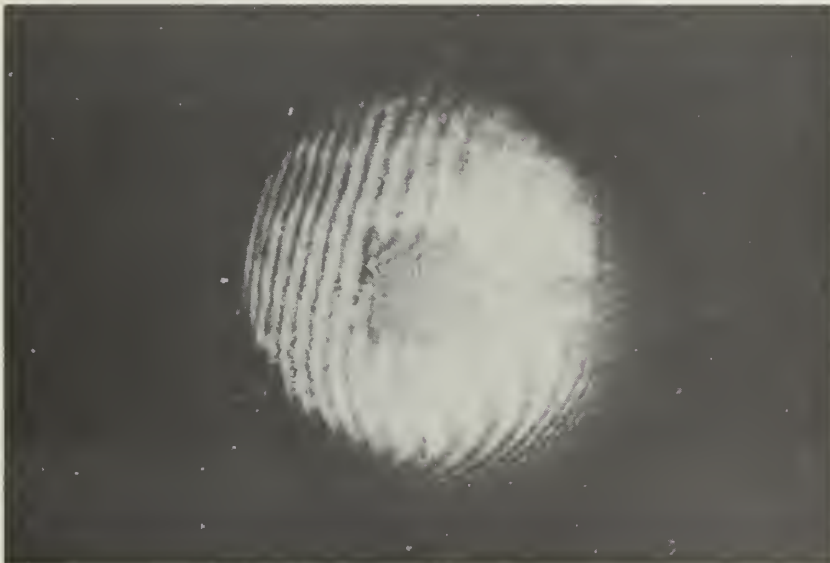
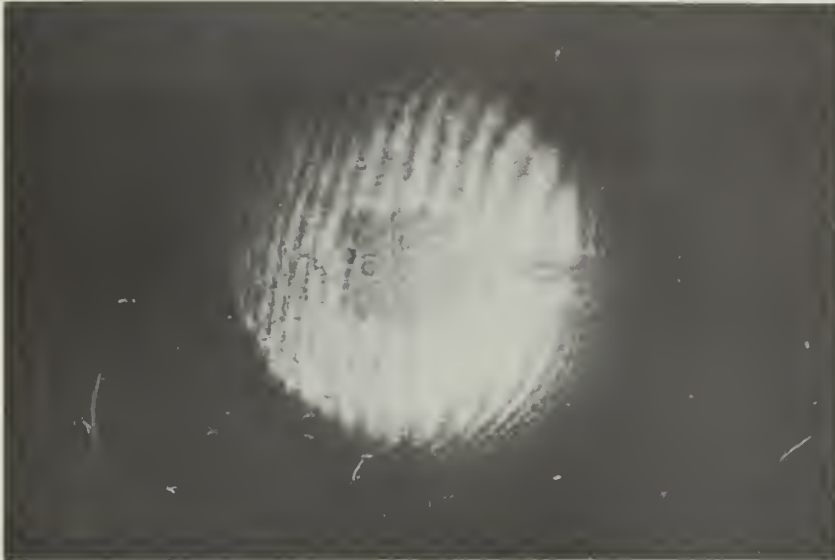


Figure 12. Sequence A Fringe Patterns. These consecut
photographs will be analyzed in the followin
figures: Figs. 15
18
22
25



Figure 13. Sequence B Fringe Patterns. These three consecutive photographs will be analyzed in the following figures:

Figs. 16
19
23
25

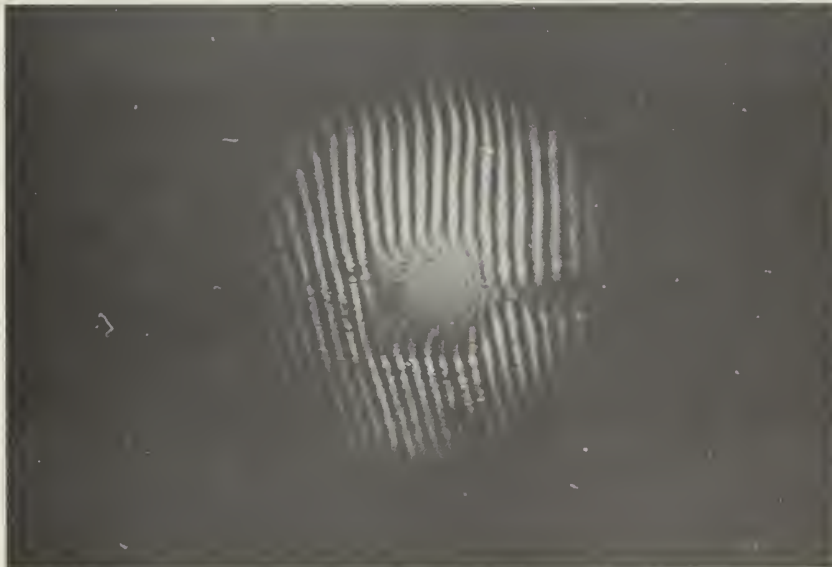
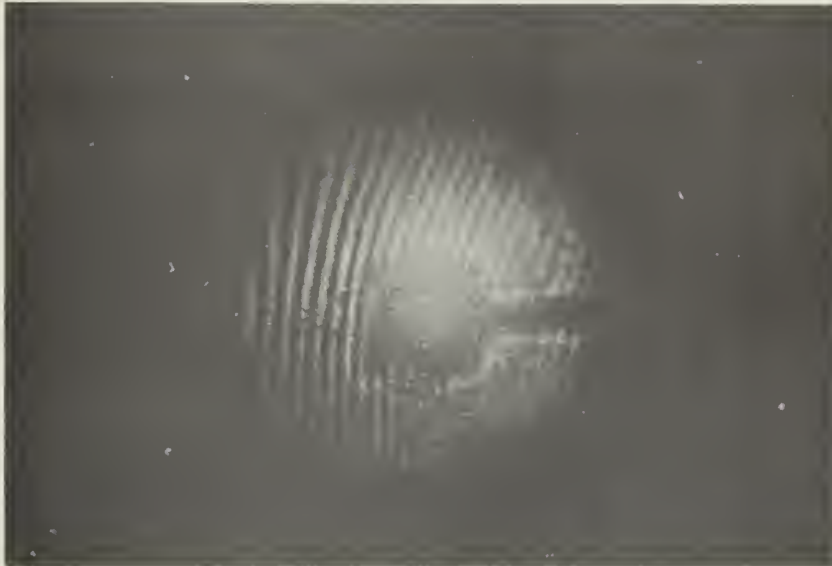


Figure 14. Sequence C Fringe Patterns. These consecutive photographs will be analyzed in the following figures: Figs. 17
20
24
27

comes

$$I(\bar{\rho}) = \frac{1}{2\eta} \left\{ \left| \underline{U}_2 \right|^2 + N^2 + u^2 L^2 \left| \underline{U}_1 \right|^2 e^{2X(\bar{\rho})} + 2uL \left| \underline{U}_1 \right| \left| \underline{U}_2 \right| e^{X(\bar{\rho})} \cos \left[\frac{2\pi \ell x}{\lambda} - \phi(\bar{\rho}) - \alpha \right] \right\} \quad (12)$$

where

α = the phase angle between \underline{E}_1 and \underline{E}_2

$$\sin \ell = |\beta_\rho| / |\beta| \simeq \ell$$

and

$$\ell \ll 1$$

It can be seen that the fringes are caused by the phase modulated sinusoid riding on the intensities of the individual signals.

Further, it can be seen that if the period of the sinusoid, $\frac{\lambda}{\ell}$, is small compared to the distance over which significant changes occur in the values of $\phi(\bar{\rho})$, the phase distortion, individual fringe lines will not experience much perturbation. Since a maximum of twenty lines distributed over the three inches of aperture show appreciable perturbations of the fringe lines, a minimum significant distance in $\phi(\bar{\rho})$ can be estimated at $(3/20)$ inches = 4 millimeters. This rough estimate of significant dimensions in $\phi(\bar{\rho})$ conforms to data given in the literature and general experience from longer paths.

The amplitude scintillation in the three sets of fringe patterns does not appear to be severe, but this is due to a selection process for just this quality.

Another notable feature of these slides is the spatially varying fringe pattern across the aperture. The fringe spacing in Figs. 12 and 13 are narrower on the left side of the aperture. Especially in the photographs of Fig. 13, one can see that the

fringe spacing not only varies spatially, but also changes radically from one photograph to the next. The photographs in Fig. 14 show a rotation of lines between photographs. The photographs of Fig. 12 were taken just prior to those in Fig. 13, while those in Fig. 14 were taken on another night without any appreciable modification of the system having taken place.

A photograph of the system through a non-atmospheric path could not be obtained unless the system as installed was changed significantly. The divergence of the wave emerging from the laser or laser-collimator when beamed into the receiver telescope was such that its focusing point was moved too far out to use the camera eyepiece as mounted. This camera eyepiece was needed to match curvatures with the LO wave. Other eyepieces required optics in the LO path. When the divergence was reduced so that the system could be used "as is", the aperture was not fully illuminated, and very little of the aperture could be seen around the secondary mirror. Thus system effects can not be directly taken out. However, the availability of consecutive photographs allows analysis of the changes in successive photographs. The optical system is the same between photographs except for advancing the film in the camera, so that changes in the fringe spacing would indicate atmospheric effects. For this reason, the photographs of Fig. 14 were included to obtain another consecutive look at the lumped system-atmospheric effects on a night different from that of Figs. 12 and 13.

3 - 1 Full Aperture Analysis

In an effort to obtain a feel for the processes that occur over the entire aperture, the slides were projected on a screen

and scanned with a television camera. The output of the television camera was displayed on an oscilloscope using the first of the methods described in section 2-4. This method is essentially the construction of a television picture but with the shades of grey replaced by vertical deflections on the individual scan lines. This method gives the appearance of a three dimensional map of the intensity over the aperture and the results are shown in Figs. 15, 16 and 17.

The main interest in displaying in this manner is to get some feel for

- (1) Phase changes along the fringes
- (2) Phase changes across the fringes
- (3) Scintillation
- (4) Systematic effects

The deep troughs on the edges of the photographs in Figs. 15, 16 and 17 are the locations of black non-reflecting tape put on the projection screen to aid in centering the picture. In every photograph, the fringe spacing increases towards the right. This is considered a system constant and as such will be discounted in further analysis.

The fringe lines tend to curl towards the lower right-hand corner. This curl is stronger in the lower half of the aperture and can be seen particularly well in photograph of Fig. 17. This is an example of the phase distortion along the fringe lines. A slightly different effect is the amplitude modulation along the fringe lines caused by phase distortion.

The scintillation can be seen best on the peak lines as on amplitude modulation. Where the modulation produced by the fringes is shallow, generally on the right hand sides of the photographs,

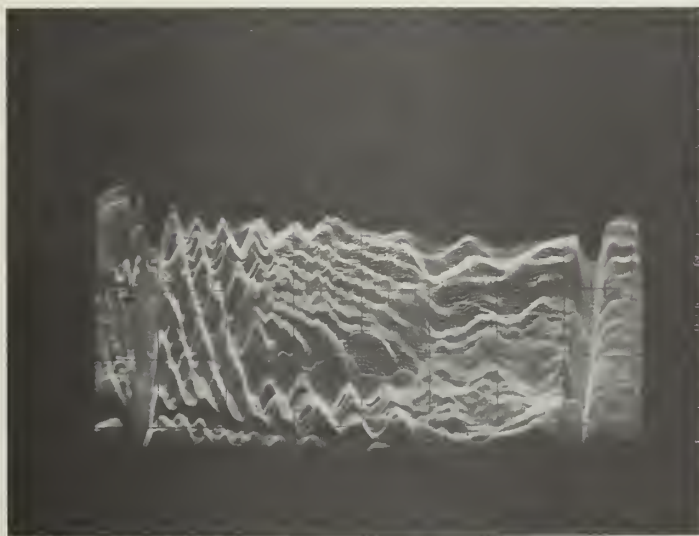
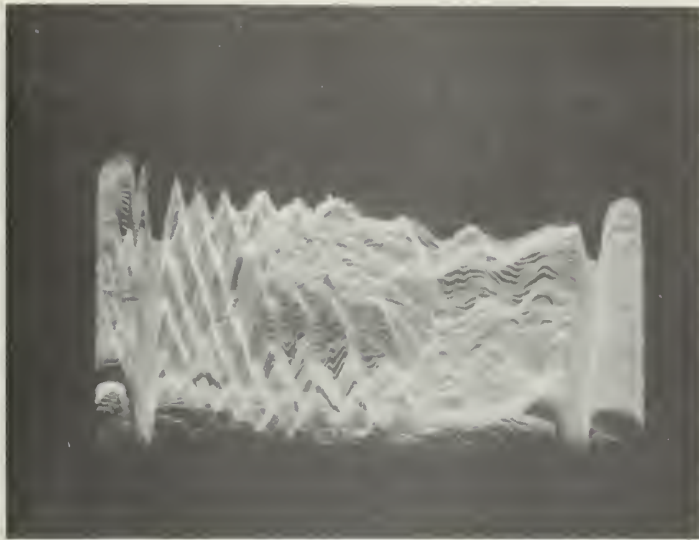


Figure 15. Sequence A Full Aperture Display of the Fringe Pattern of Photograph #1 and #2 by Method of Section 3-2.



Figure 16. Sequence B Full Aperture Display of the Fringe Pattern of Photograph #1 by Method of Section 3-2.



Figure 17. Sequence C Full Aperture Display of the Fringe Pattern of Photograph #1 by Method of Section 3-2

scintillation tends to swamp out the detail of the pattern.

The analysis of the phase process across the fringe grain will be done in detail in the next two sections. It is worthwhile noting at this point that the fringe pattern is generally visible and enough definition exists to justify a look in detail.

3 - 3 Phase Analysis

Using equation (B-2) as the model for this fringe line system, the intensity is

$$I(\bar{\rho}) = \frac{1}{2\eta} \left\{ \left| \underline{U}_2 \right|^2 + N^2 + \mu^2 L^2 \left| \underline{U}_1 \right|^2 e^{2X(\bar{\rho})} + 2\mu L \left| \underline{U}_2 \right| \left| \underline{U}_1 \right| e^{X(\bar{\rho})} \cos \left[\frac{2\pi \ell x}{\lambda} - \phi(x, y_0) - \alpha \right] \right\} \quad (12)$$

If a narrow strip in the y dimension is examined, narrow enough so that the processes do not change with y, the intensity expression becomes

$$I(x, y_0) = \frac{1}{2\eta} \left\{ \left| \underline{U}_2 \right|^2 + N^2 + \mu^2 L^2 \left| \underline{U}_1 \right|^2 e^{2X(x, y_0)} + 2\mu L \left| \underline{U}_2 \right| \left| \underline{U}_1 \right| e^{X(x, y_0)} \cos \left[\frac{2\pi \ell x}{\lambda} - \phi(x, y_0) - \alpha \right] \right\} \quad (13)$$

Assuming that the spatial sinusoid is visible despite the random amplitude modulation from scintillation, the distance between successive peaks or valleys can be measured. This indicates the sinusoid argument going through 2π radians or one period. Thus, choosing the peak lines as the point to measure period length on, we know over one period

$$\left[\frac{2\pi \ell x}{\lambda} - \phi(x, y_0) \right] - \left[\frac{2\pi \ell x'}{\lambda} - \phi(x', y_0) \right] = 2\pi \quad (14)$$

where

x and x' are the points where two adjacent maximum values of the sinusoid are located. In the remainder of this thesis x and x' will indicate adjacent maxima.

Since x and x' can be measured, we get

$$\phi(x, y_0) - \phi(x', y_0) = 2\pi \left[\frac{\ell}{\lambda} (x - x') - 1 \right] \quad (15)$$

Thus over the distance $(x - x')$ we get a measure of how the phase distortion process acted. If we continue this analytic procedure across the fringe pattern, we have some notion of how $\phi(x, y_0)$ changes with x .

It has been shown by Fried that geometrical interpretations can be placed on the form of $\phi(x, y_0)$. If a Taylor type expansion is made of $\phi(x, y_0)$, we get

$$\phi(x, y_0) = A + Bx + Cx^2 + \dots \quad (16)$$

Putting this expression for $\phi(x, y_0)$ into Eq. 13 gives

$$I(x, y_0) = \frac{1}{2\eta} \left\{ \left| \underline{U}_1 \right|^2 + N^2 + u^2 L^2 \left| \underline{U}_1 \right|^2 e^{2X(x, y_0)} + 2uL \left| \underline{U}_1 \right| \left| \underline{U}_2 \right| e^{X(x, y_0)} \cos \left[\frac{2\pi \ell x}{\lambda} - \alpha - A - Bx - Cx^2 \dots \right] \right\} \quad (17)$$

Here it can be seen readily that

A represents a phase origin relative to the position coordinates x

Bx represents a linear phase change, a tilt relative to the direction of travel

$Cx^2 \dots$ represents a spherical phase change, representing a spherical wavefront on the received wave

and the coefficients give a good measure of the importance of each term; the number of terms needed to adequately represent the phase process indicate in some sense how simple the phase changes are.

There are two problems involved with applying this analysis directly to the fringe patterns made for this thesis. The first is that no non-atmospheric pattern exists to take out the purely

systematic effects. The only method of removing these systematic effects is to examine consecutive patterns and remove the constant effects; this leads to the second problem. The only distinctive feature that can be used for locating the same narrow strip in consecutive patterns is the secondary mirror. Thus without taking data for several entire slides, which would take a prohibitive amount of time, only limited strips can be handled in each pattern for comparison with the next. Fortunately, the regions just above and below the secondary mirror are not unique compared to the remainder of the fringe patterns in the rest of the aperture, as can be seen by examining Figs. 12, 13 and 14. Thus these regions are a reasonable choice for analysis.

4 - Narrow Strip Analysis

To examine how the fringe patterns made for this thesis changed in phase, narrow strips above and below the secondary mirror were measured in detail. The slides containing the fringe patterns were projected on a screen, then scanned using the television camera. The fringes were aligned so that the horizontal scan of the television camera was across the grain of the fringe pattern. Selected horizontal lines from the television camera were displayed and the locations of the peaks of the fringe lines were measured for five to fifteen successive horizontal lines. This corresponds to a strip one to three millimeters wide over the objective aperture. Typical displays of these horizontal lines are shown in Figs. 18, 19 and 20, where the top line corresponds to a scan line in the top half of the fringe pattern; the middle line to a scan line in the middle, and the bottom line to a scan



Figure 18. Sequence A
Typical Horizontal Lines
from Television Camera
for Photograph #1



Figure 19. Sequence B
Typical Horizontal Lines
from Television Camera
for Photograph #1

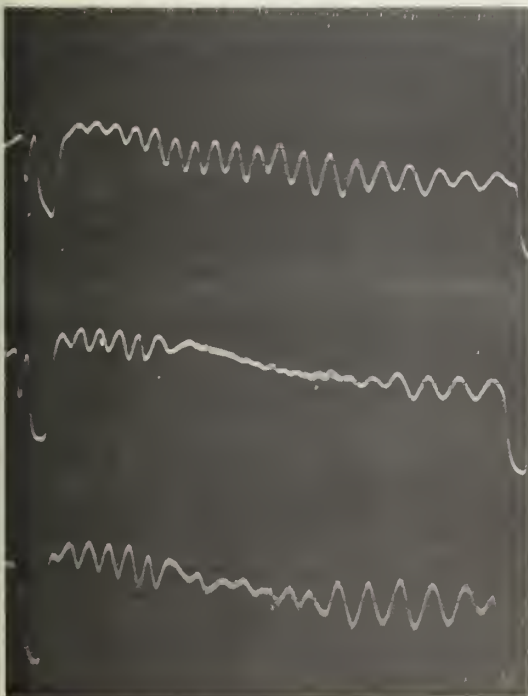


Figure 20. Sequence C
Typical Horizontal Lines
from Television Camera
for Photograph #1

line in the bottom half of the fringe pattern. The relatively small modulation in the middle of the middle lines is due to the secondary mirror. The relatively deep excursion of the scan lines at the edges is caused by black non-reflecting tape placed on the screen to provide a means of centering the fringe pattern on the television monitor. The spatial scale of the oscilloscope display can be related directly to the spatial scale of the aperture. The conversion is 0.40 inches of aperture is equal to 1 centimeter of oscilloscope display. This conversion will be applied to all future figures that deal with the aperture.

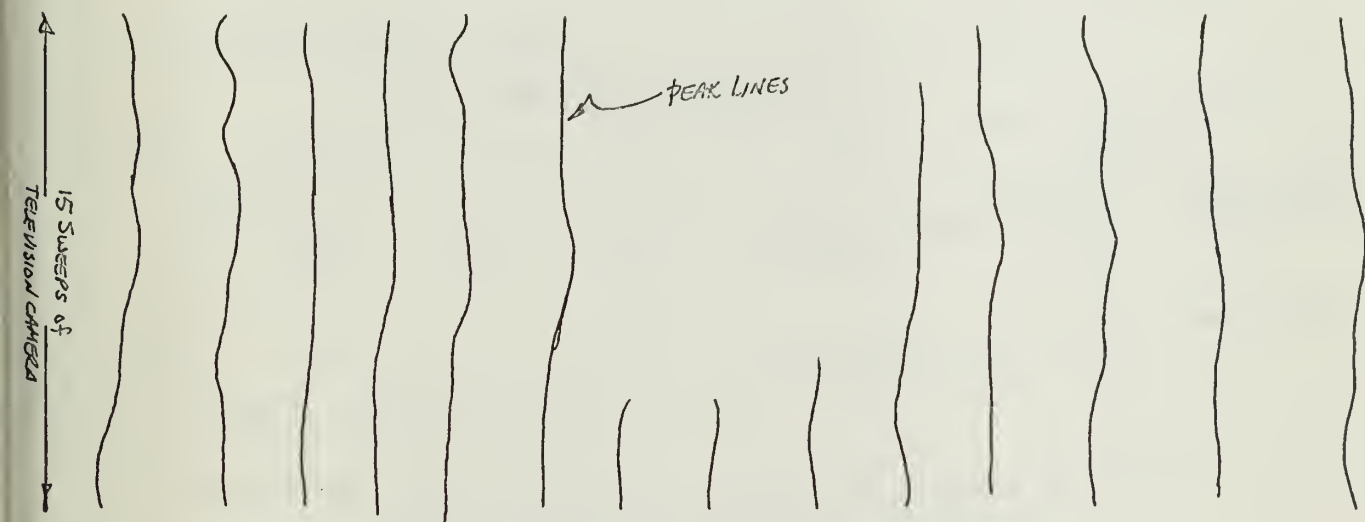
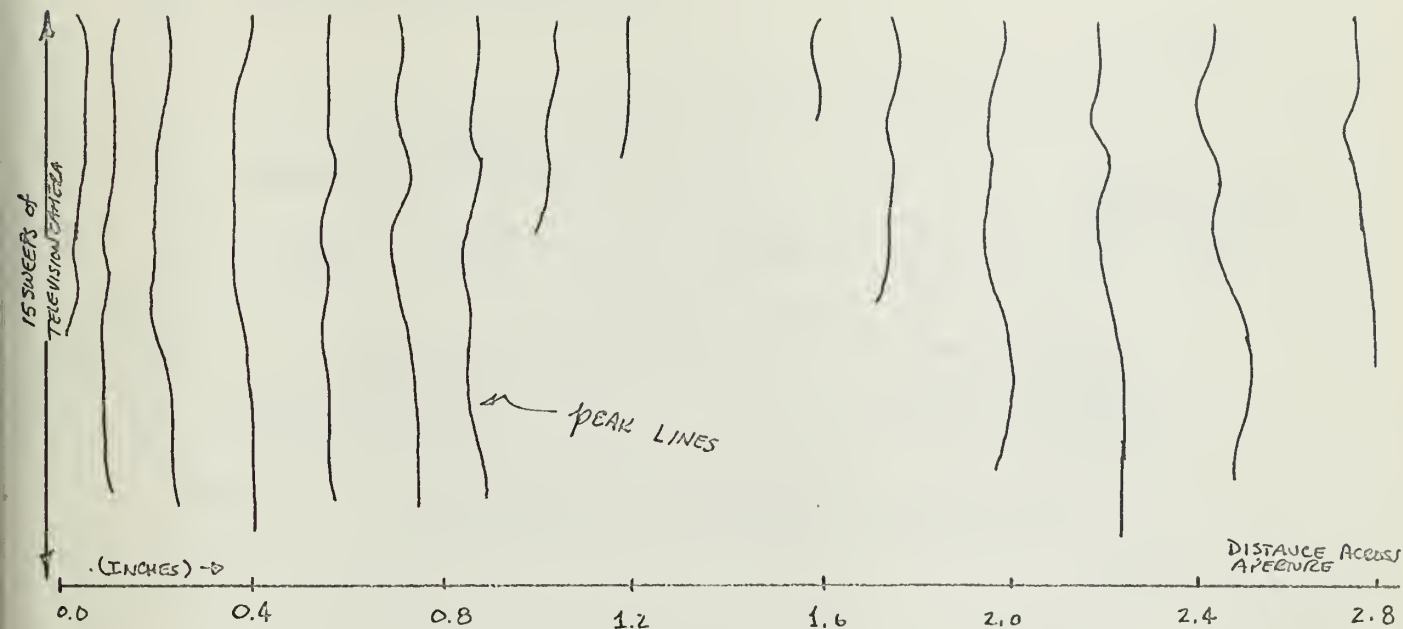
Typical unaveraged strips are shown in Fig. 21, where the peak lines are drawn in. The locations of these lines are simply averaged along the fringes. The distance between the averaged locations of the peak lines across the aperture is plotted in Figs. 22, 23 and 24. From Eq. 15 this distance between peak lines can be related to the phase distortion and fringe period as

$$(x-x') = \frac{\lambda}{2\pi\ell} [\phi(x, y_0) - \phi(x', y_0) + 2\pi] \quad (18)$$

Thus measuring $(x-x')$ gives a number proportional to ϕ over the distance $(x-x')$. Further geometric interpretations about the form of ϕ can be made as successive $(x-x')$ values are measured and plotted across the aperture. A direct measure of the spatial frequency $\frac{\ell}{\lambda}$ is not available, however this term can be assumed constant across the aperture. Then any changes in the $(x-x')$ across the aperture can be attributed to changes in $\phi(x, y_0)$ and any changes in $(x-x')$ between photographs can also be attributed to the change in $\phi(x, y_0)$ with time.

This method of plotting the average distance between peaks

ABOVE THE SECONDARY MIRROR



BELOW THE SECONDARY MIRROR

Figure 21. Typical Unaveraged Locations of the Peaks of a Fringe Pattern. This example comes from Photograph 1 of Sequence B.

AVERAGE DISTANCE BETWEEN PEAKS
OF FRINGE PATTERN (MILLIMETER UNITS)

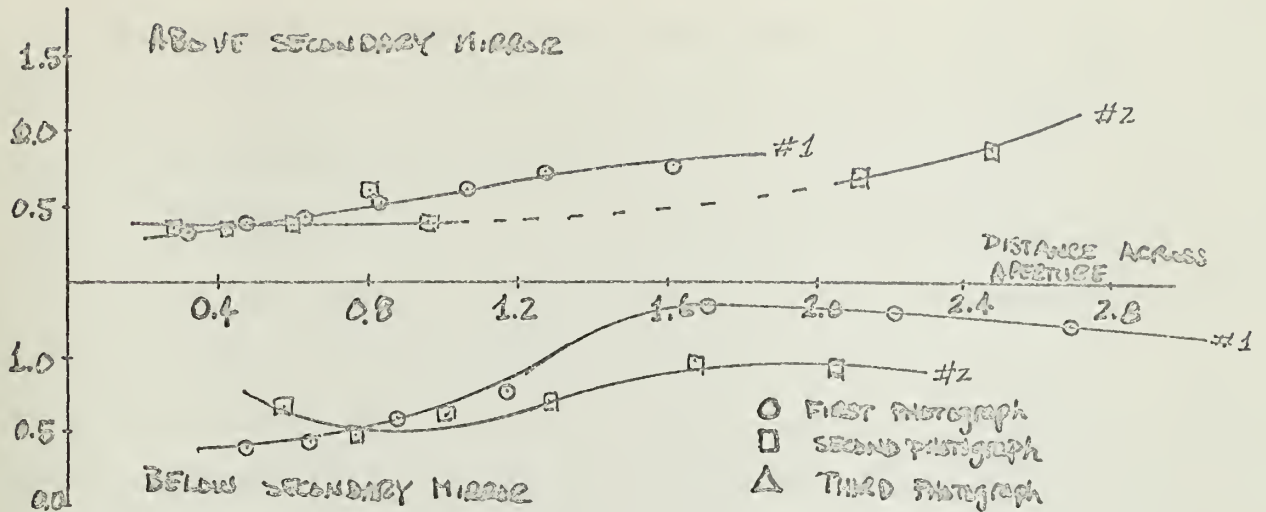


Figure 22. Average Spatial Period of Fringe Pattern over Objective Aperture Sequence A

AVERAGE DISTANCE BETWEEN PEAKS
OF FRINGE PATTERN (MILLIMETER UNITS)

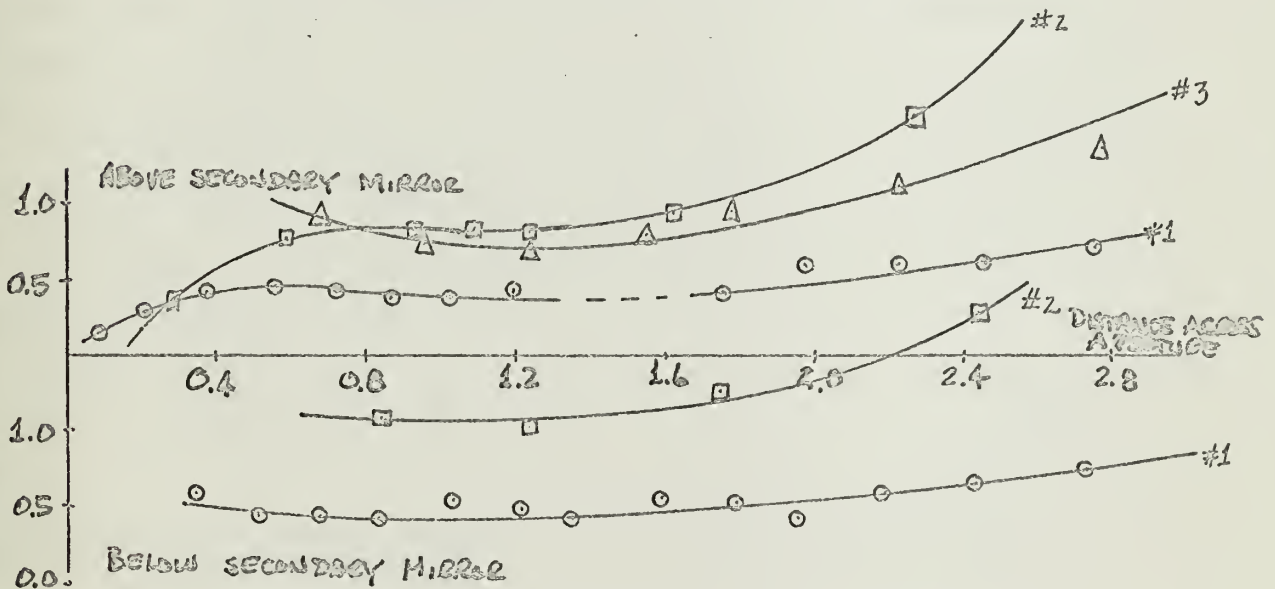


Figure 23. Average Spatial Period of Fringe Pattern over Objective Aperture Sequence B

AVERAGE DISTANCE BETWEEN PEAKS
OF FRINGE PATTERN (MILLIMETER UNITS)

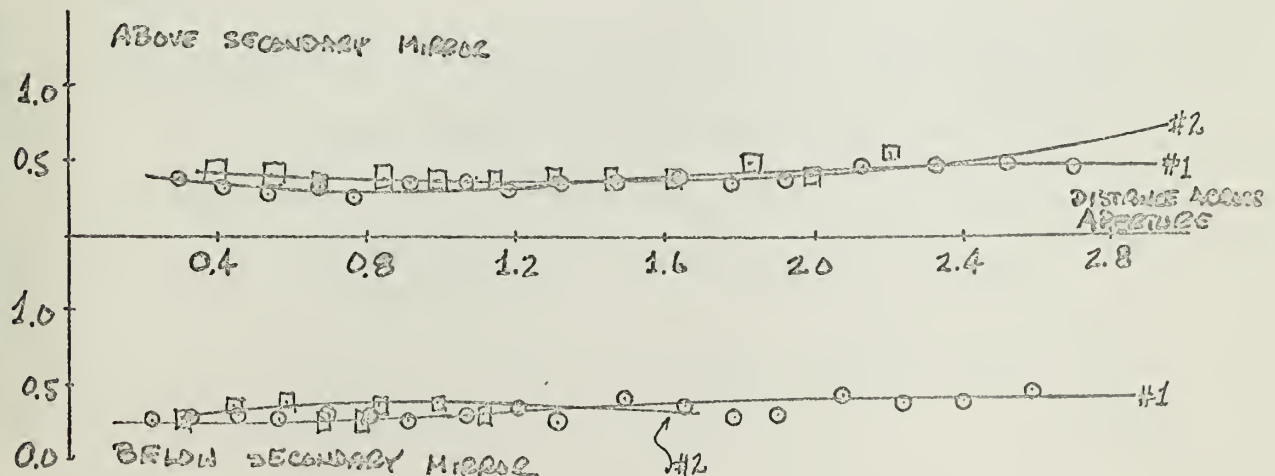


Figure 24. Average Spatial Period of Fringe Pattern over Objective Aperture Sequence C

gives a visual display of the general type curvature of the phase process across the aperture and seems to show a general quadratic form indicative of spherical distortion of the incoming wave.

Another method of plotting is to use the averaged location of the peak lines on the abscissa and to plot the 2π radian change of the sinusoid argument between successive peaks on the ordinate. This is shown in Figs. 25, 26 and 27. These graphs have a linear mean square estimate line plotted for reference. The first aspect to note is the dominance of the linear term in every plot. The lines have some higher order deformations, but the linear term is obviously most important. The second aspect to note is the change in slope between photographs in Fig. 26. This means a significant change in tilt of the incoming wave has taken place. We can equate the argument of the sinusoid in Eq. 13 to the estimate lines in Figs. 25, 26 and 27 as

$$\left[\frac{2\pi \phi_0 x}{\lambda} - \phi(x, y_0) - \alpha \right] = k_1 x + k_2 \quad (19)$$

where

$$k_1 = \frac{\mu_{11}}{\sigma_x^2} \quad \text{the linear estimate line slope measured for each photograph}$$

μ_{11} the covariance between the averaged location of the peak lines, x , and the total phase change, y , at that x

σ_x^2 the variance of the averaged location of the peak lines

m_x the mean of the averaged locations of the peak lines

m_y the mean of the total phase change across the aperture

$$k_2 = m_y - \frac{\mu_{11}}{\sigma_x^2} m_x \quad \text{the linear estimate intercept for a photograph}$$

The change of this argument between successive photographs is

$$\phi(x, y_0) - \phi'(x', y_0) = (k_1 - k'_1)x - (k_2 - k'_2) \quad (20)$$

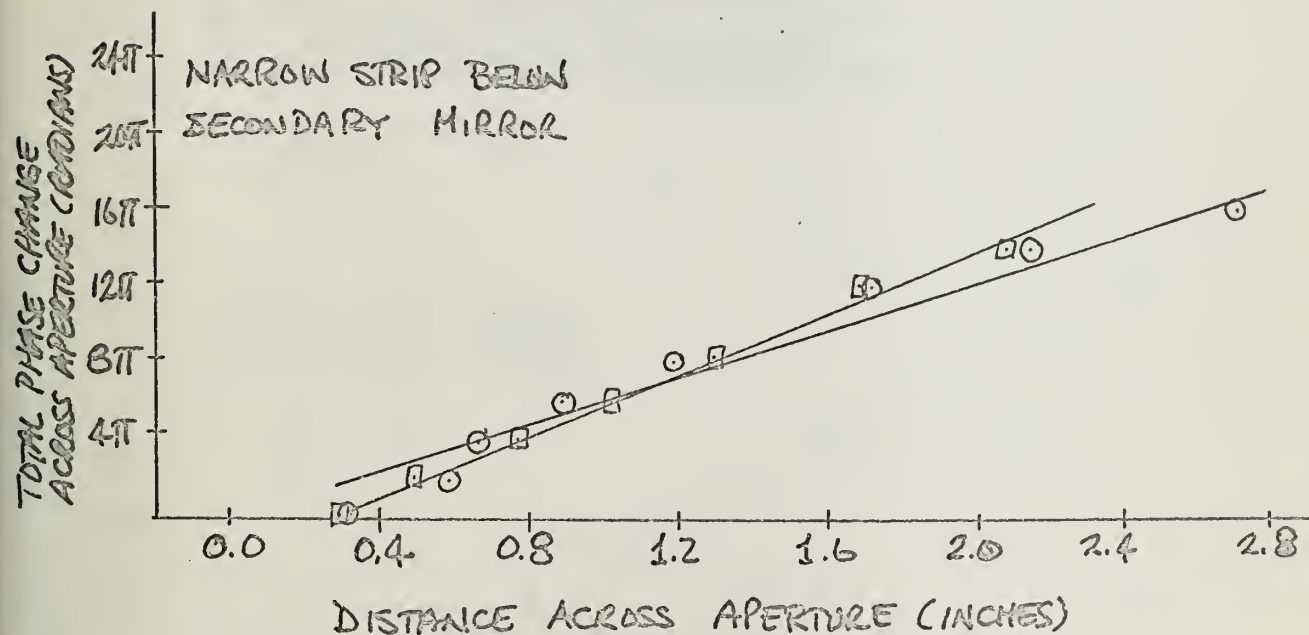
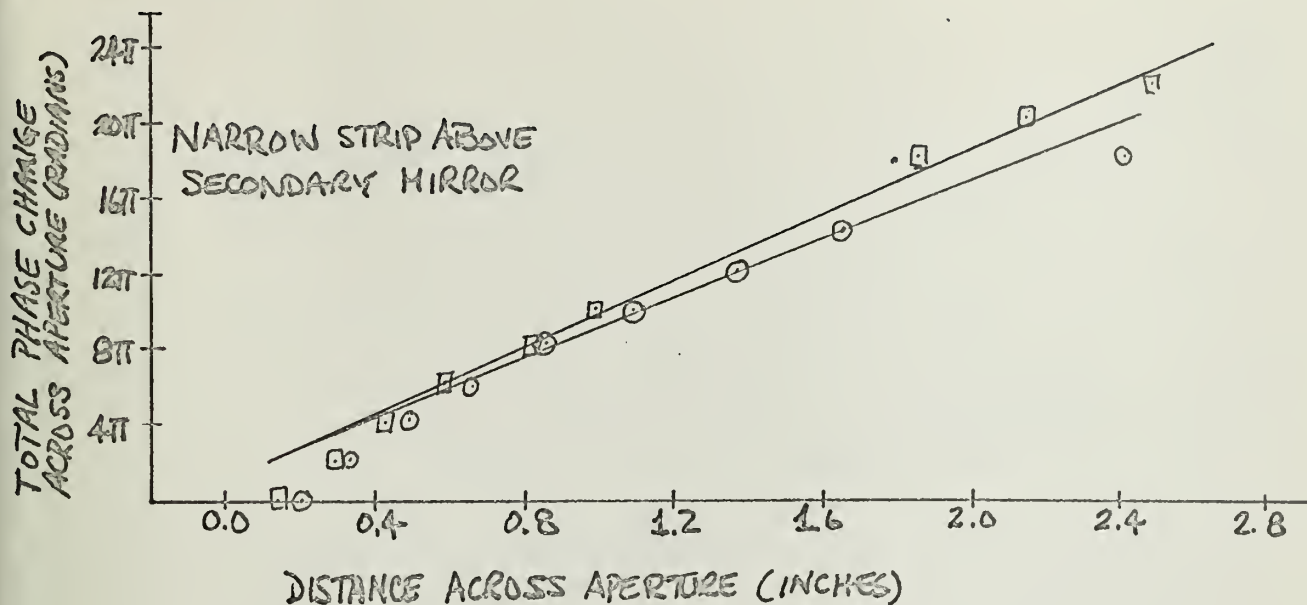


Figure 25. Total Phase Change Across the Receiving Aperture Sequence A

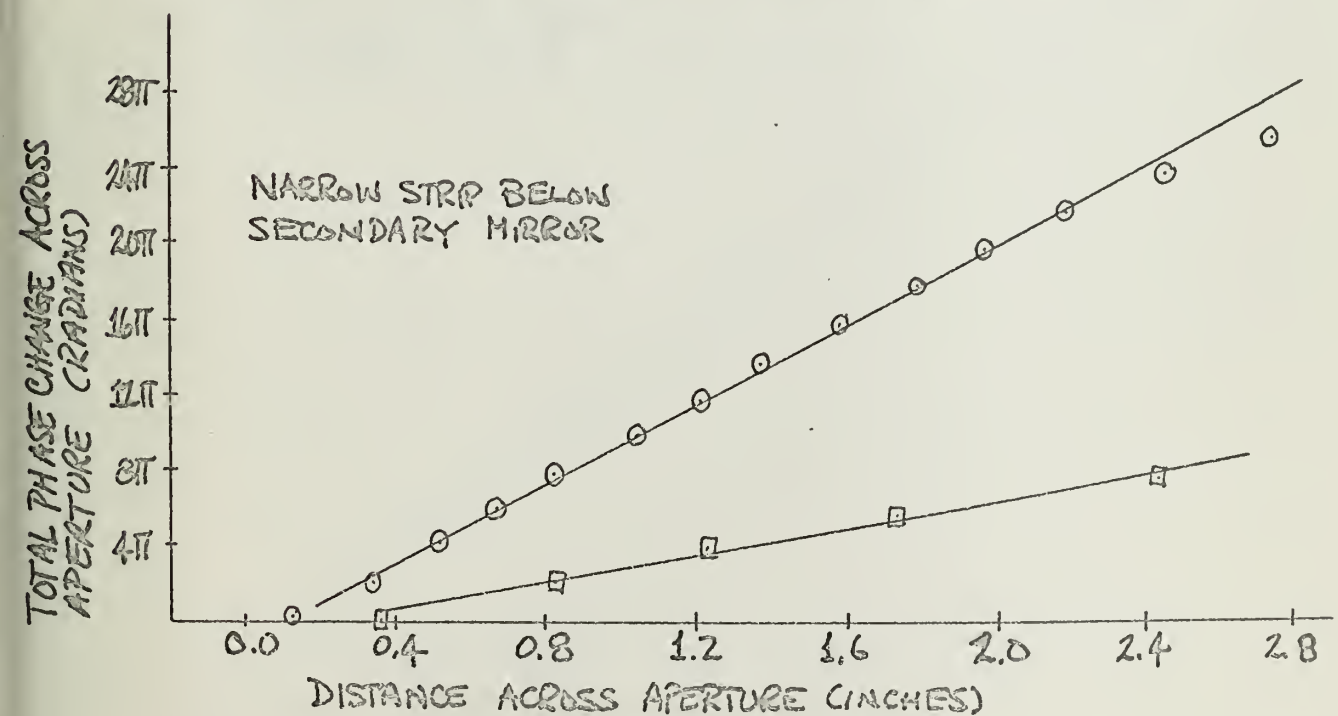
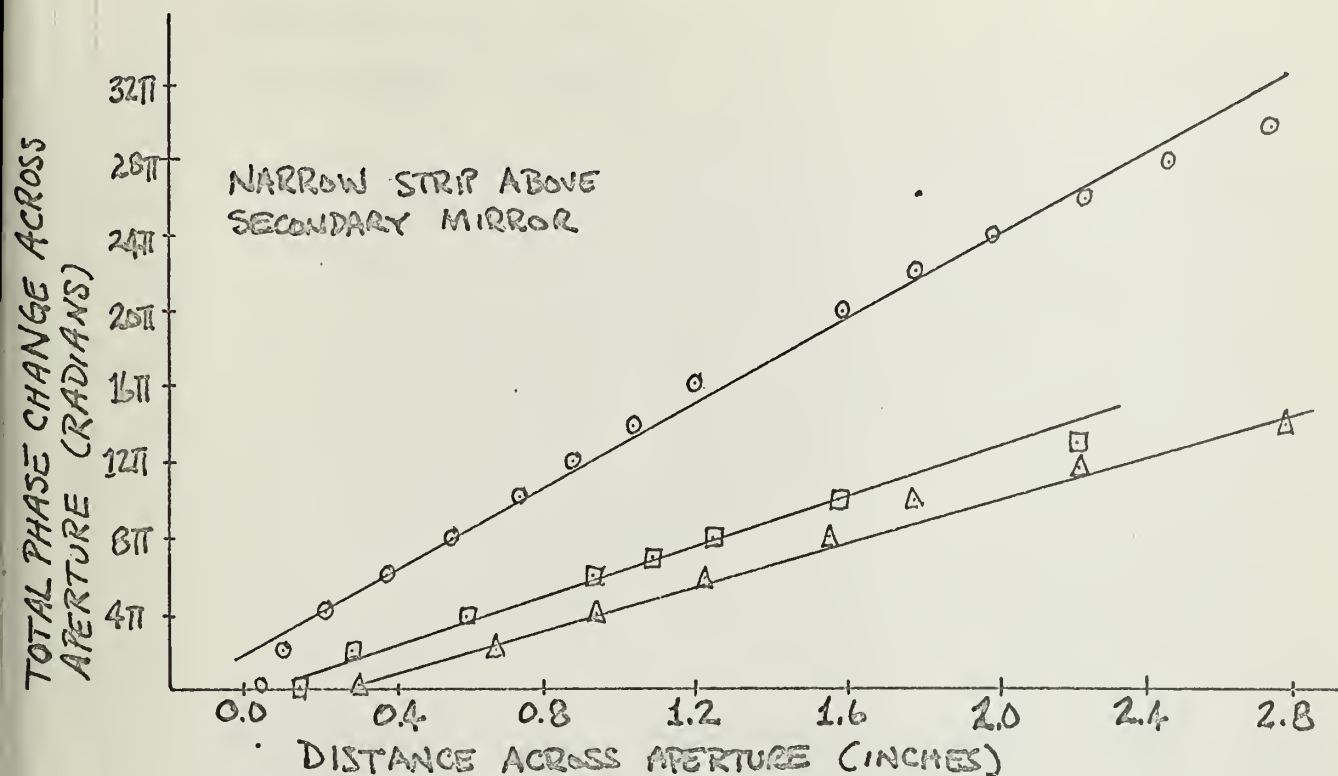
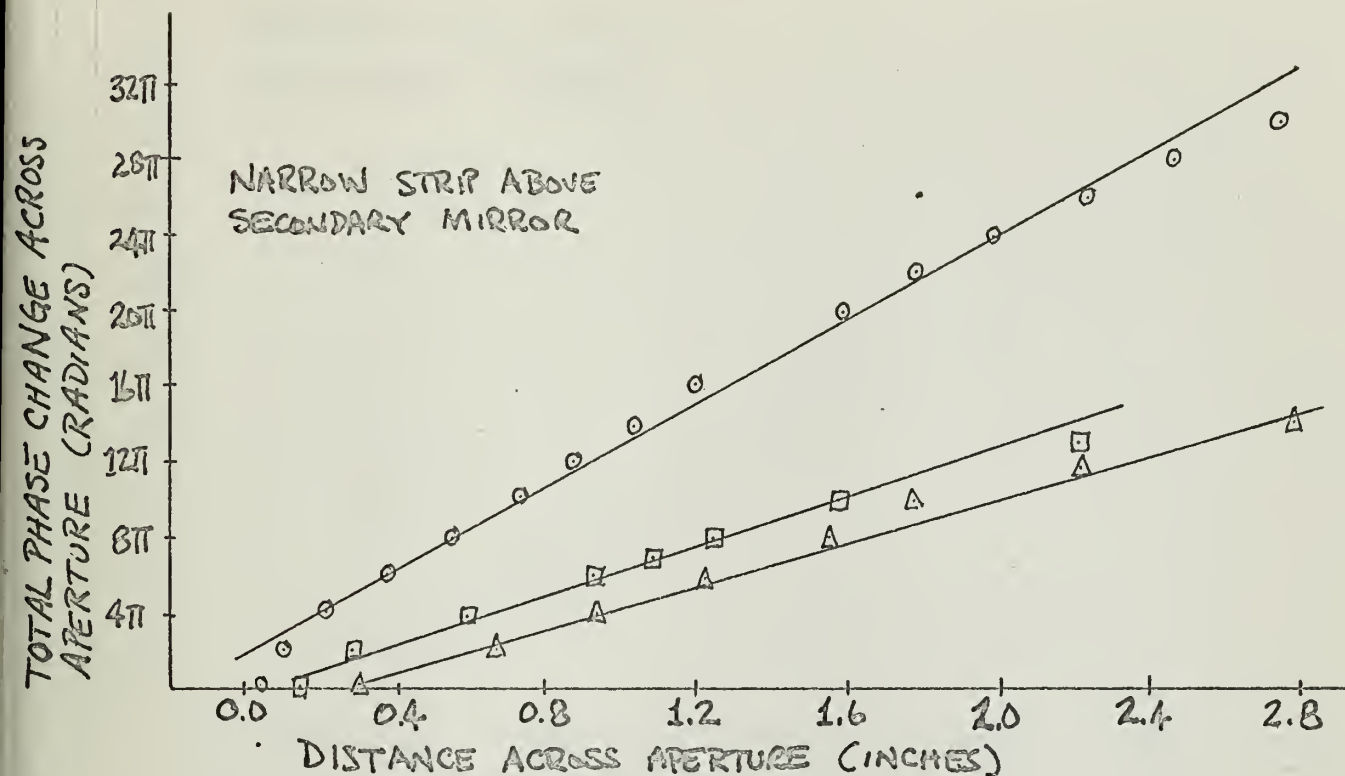


Figure 26. Total Phase Change Across the Receiving Aperture Sequence B



○ DATA POINTS FROM FIRST PHOTOGRAPH
 □ DATA POINTS FROM SECOND PHOTOGRAPH
 △ DATA POINTS FROM THIRD PHOTOGRAPH

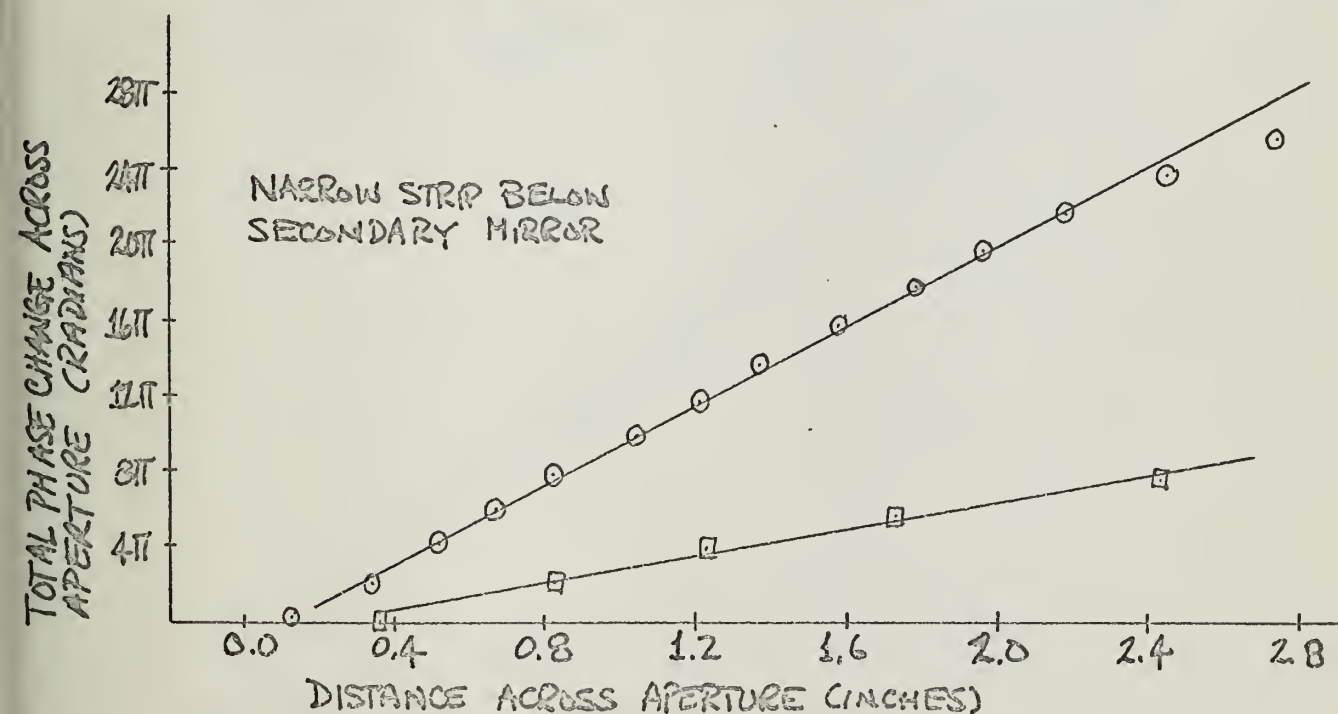


Figure 26. Total Phase Change Across the Receiving Aperture Sequence B

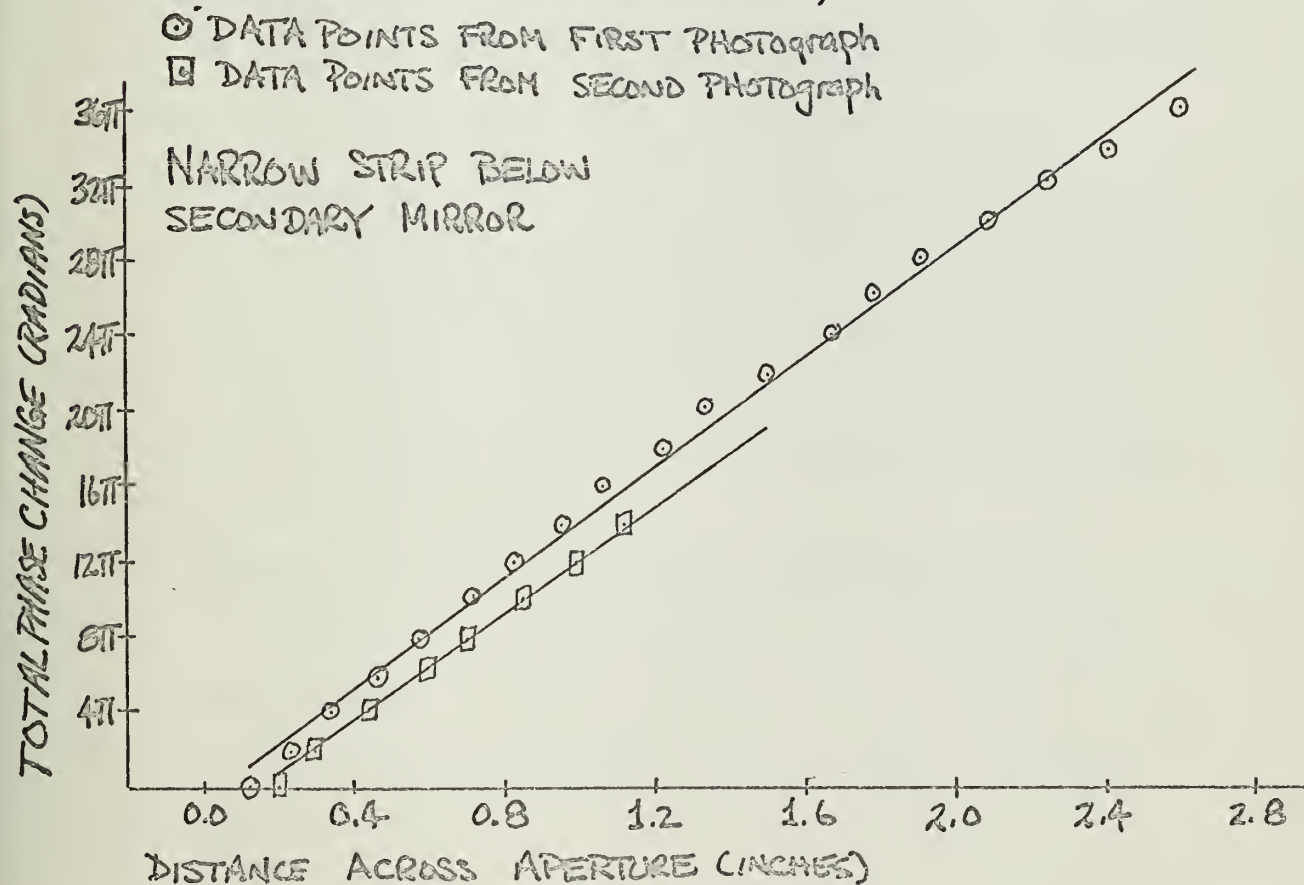
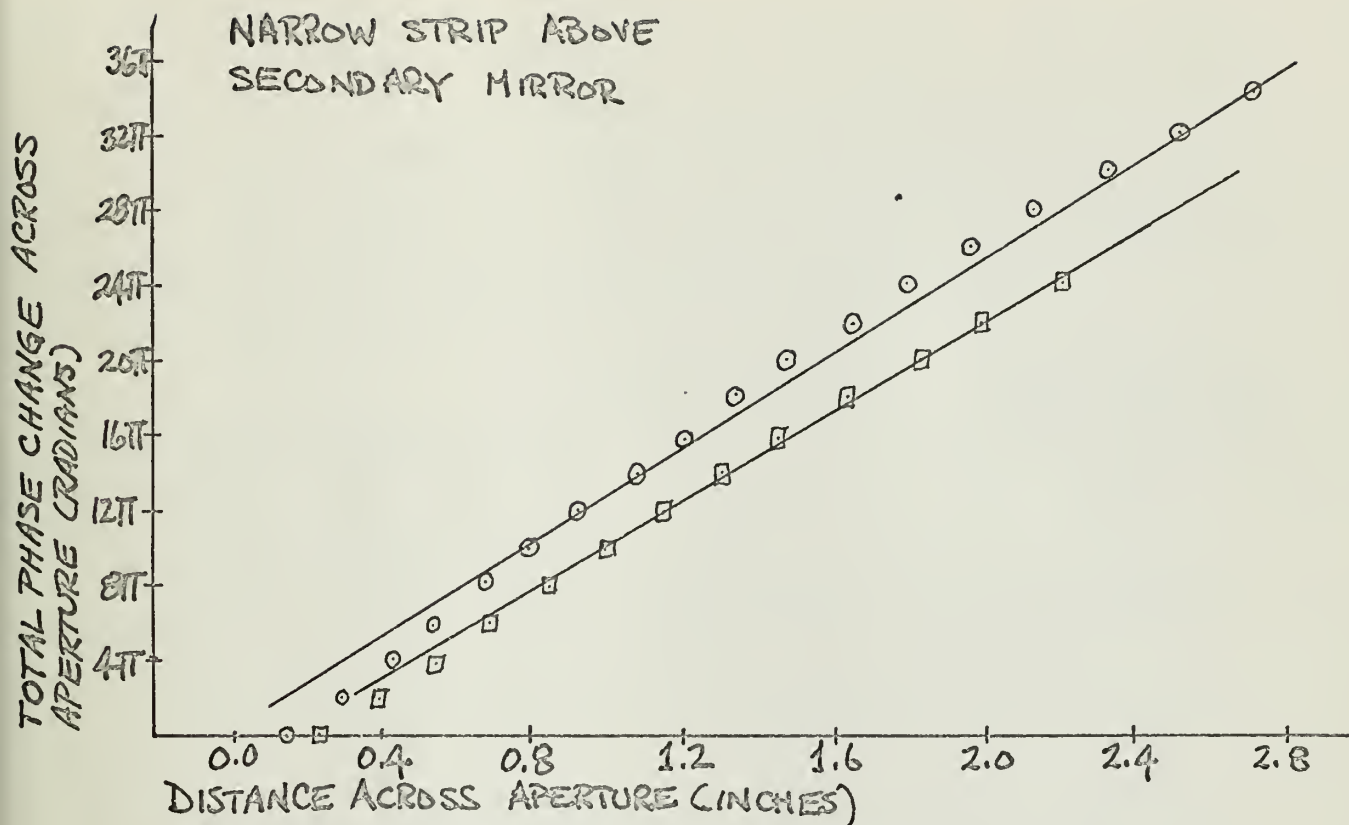


Figure 27. Total Phase Change Across the Receiving Aperture Sequence C

where the primes refer to the succeeding photograph. The $(k_2 - k'_2)$ is not meaningful since many steps in the analysis introduce arbitrary references in phase. However, the change in slope is easily measured. These changes in k_1 are shown in Table 1 and the equivalent change in tilt of the incoming wave is also listed.

	Δk (radians/inch)	Tilt change (in seconds of arc)
Figure 25	Above secondary mirror 1.2π	3.08
	Below secondary mirror 2π	5.15
Figure 26	Above secondary mirror $4.25\pi/.75\pi$	10.9/1.925
	Below secondary mirror 8.75π	22.5
Figure 27	Above secondary mirror $.15\pi$.386
	Below secondary mirror $.75\pi$	1.925
Table 1 Measured Changes in Tilt in Three Sets of Consecutive Photographs (from Figs. 12, 13 and 14)		

As is discussed in Appendix A, tilt changes less than 15 microradians (3.2 seconds of arc) will be indistinguishable from possible mirror tilt caused by vibrations. This limit is exceeded only in Fig. 26. If the photographs used to generate Fig. 26 are reexamined (see Fig. 13), it can be clearly seen that the fringe spacing changes dramatically from the first to second photograph, an effect not seen in Figs. 12 and 14.

In an effort to determine the higher order deformations, a log-log plot was constructed using the average location of peak lines as the abscissa and the phase changes, with the linear estimate subtracted out, as the ordinate. However, only systematic effects are visible.

CHAPTER 4

This chapter summarizes the results presented in Chapter 3, and draws some conclusions about the general procedure. Some suggestions for improvement of this system are also made.

4 - 1 Conclusions

Using the methods outlined in Chapter 3, it is clearly possible to measure phase in a narrow strip across the objective aperture. Using the resulting phase plots, it is possible to compute a change in tilt between successive photographs. In this experiment, the linear terms and systematic effects masked possible higher order deformations caused by atmospheric turbulence, but with more care on a longer path these effects should be measurable.

The details of the analysis show that the minimum tilt changes, separate from mirror induced tilt, measurable by the present system was approximately 5 seconds of arc. It is interesting to note that the measured tilt ranged as high as 22.5 seconds of arc, a large value for a three inch aperture and a short path.

When the fringe pattern produced by the two beams is looked at through a Wratten filter, the system dynamics can be seen graphically. The fringe lines waver along their length and, as their spacing gets wider, a bowing travelling across the pattern is often seen. A third effect is a shimmering of the entire pattern, possibly indicating a time change of phase origin suggested in section 3-3.

The system of oscilloscope display and visual reading is clearly a tedious method of data taking. The amount of data that can be taken in this way is small, and is not compatible

with machine computation. Judgement can be exercised to pick out the peak lines from scintillation when this display method is used, but the peaks and valleys of the fringe pattern are the only parts that can be used for visual data taking.

The lack of a system-only series of photographs was a hindrance to the analysis. Some further feel for the motions of the down-range reflector would have been invaluable in interpreting the results.

4 - 2 Suggestions for Improvement

The first suggestion would be to set up a path in the laboratory long enough so that the divergence of the wave entering the telescope is not too fast. At the same time, the beam should illuminate a large amount of the aperture. Thus, using the same system as one would use when taking atmospheric data, a recording of the system alone could be made. This would be most helpful in analyzing single photographs, and sequences would not be necessary.

A second suggestion is to convert the video output of the television camera to digital data for later machine analysis. The basic equipment is available, and only a gating circuit and sam-logic pling sequence/need be added. The master clock that generates the pulse train used to synchronize the television camera runs at 110,250 Hz; the first frequency used in the television synchronization is at 15750 Hz. The sampling pulses could be selected to run off this master clock with some flexibility as to the desired frequency, and synchronization with the television camera could still be retained. With the data in digital form on tape, a digital computer could be used to analyze the data, allowing a de-

tailed analysis over the entire aperture.

As longer paths are used, the problem of reflector induced tilt would be lessened. The increase in beam diameter would not be too large as path length is extended, but beam motion due to reflector tilts would be more apparent. The motion of the beam could be observed and data could be taken only when the beam is steady on the target. Thus mirror induced tilt would be minor.

APPENDIX A

This appendix contains an analysis of the heterodyning system in more detail than in Chapter 2, a fuller explanation of the data analysis system, and electronic circuit diagrams.

A - 1 Heterodyne System Analysis

The scheme outlined in Figure 2 for creating a spatial interference pattern proportional to the phase distortion process caused by atmospheric turbulence can be analyzed using simple models.

The front end of the laser (typically the output of the Spectra-Physics Model 119 laser would be 0.1 milliwatt at the front end and 10 microwatts at the back end) is collimated and transmitted through the turbulent atmosphere and then reflected back over the same path by the down range reflector. After collection by the receiving telescope this signal is mixed with a local oscillator signal taken from the back end of the laser. These two waves can be approximately described before transmission as plane waves of finite spatial extent. As the finite spatial extent of the fields should not cause important effects for this experiment, it is not explicitly included. Thus in complex notation

$$\underline{E}_{\text{Trans}} = \underline{U}_1 e^{-j\vec{\beta}_1 \cdot \vec{r}} e^{j\omega t} \quad (\text{A-1})$$

$$\underline{E}_{\text{Lo}} = \underline{U}_2 e^{-j\vec{\beta}_2 \cdot \vec{r}} e^{j\omega t} \quad (\text{A-2})$$

where

$$|\beta_1| = |\beta_2| = \frac{2\pi}{\lambda} = \frac{\omega}{c}$$

$$\lambda = 6328\text{\AA}$$

The atmospheric effects on the propagating beam include diffraction, scattering, and absorption losses; atmospheric turbulence modulation; beam spreading due to imperfect reflector-mirror flatness; phase modulations due to mirror motions caused by vibration. Collection of the returned beam will introduce further losses due to the finite collecting aperture which is smaller than the beam size. Background radiation will also be collected in the receiving telescope. The various effects will be described as follows:

$\gamma(\vec{r}, t)$
e represents the turbulent channel

where

$$\gamma(\vec{r}, t) = X(\vec{r}, t) + j\phi(\vec{r}, t)$$

$X(\vec{r}, t)$ represents the amplitude scintillation process

$\phi(\vec{r}, t)$ represents the phase distortion process

$L(\vec{r}, t)$ represents losses due to

1. Diffraction
2. Particle scattering
3. Molecular absorption
4. Mirror imperfections
5. Collection losses

$e^{j\psi(\vec{r}, t)}$ represents phase modulations due to mirror movements

$E_n(\vec{r}, t)e^{j\Theta_n(\vec{r}, t)}$ represents the wide bandwidth Gaussian noise collected by the receiver

Using the channel model of Chapter 1, the transmitted field will be received as

$$E_{\text{Rec}}(\vec{r}, t) = L(\vec{r}, t) U_1 e^{j\vec{\beta}_1 \cdot \vec{r}} e^{j\omega t} e^{\gamma(\vec{r}, t)} e^{j\psi(\vec{r}, t)} + E_n(\vec{r}, t) e^{j\Theta_n(\vec{r}, t)} e^{j\omega t} \quad (\text{A-3})$$

The collecting telescope will minify the portion of this re-

ceived beam within its aperture. As long as one looks "close enough" to the eyepiece, the minified image is a clean representation of illumination in the object space. (Going further away gets into the Fresnel zone of the secondary mirror and aperture edge effects.) The collected field is mixed with a local oscillator field by a beam splitter and projected on a plane screen for detection. The geometry of this plane screen (Fig. 1) is selected so that $z=0$ on the surface; the transmitted wave approaches the surface normally and the local oscillator signal approaches the surface obliquely, and thus has a direction cosine on the surface. The fields using the geometry of Figure 1 are

$$\underline{E}_{Lo}(\bar{\rho}, t) = \underline{U}_2 e^{-j\bar{\beta} \cdot \bar{\rho}} e^{j\omega t} \quad (A-4)$$

$$\begin{aligned} \underline{E}_{Trans}(\bar{\rho}, t) = L(\bar{\rho}, t) \mu \underline{U}_1 e^{j\gamma(\bar{\rho}, t) j\omega t} \\ + \mu \underline{E}_n(\bar{\rho}, t) e^{j\theta_n(\bar{\rho}, t) j\omega t} \end{aligned} \quad (A-5)$$

$$\underline{E}_{total} = \underline{E}_{Lo}(\bar{\rho}, t) + \underline{E}_{Trans}(\bar{\rho}, t) \quad (A-6)$$

where

$\bar{\rho}$ = the two-dimensional vector in the plane of the detector surface

μ = the collecting telescope-eyepiece magnification

The detector, in this case film, will measure the intensity which is

$$I_{in}(\bar{\rho}, t) = \frac{(\underline{E}_{total})(\underline{E}_{total})^*}{2}$$

Further, a black box model of this detection process includes a time averaging over the period of exposure as shown in Fig A-1.

T is the period of the shutter opening and is on the order of 2-10

iseconds for the 35mm camera. The input intensity in this

process is

$$I_{in}(\vec{p}, t) = \frac{1}{2\eta} \left\{ \underline{E}_{Lo} \underline{E}_{Lo}^* + \underline{E}_{Trans} \underline{E}_{Trans}^* + \underline{E}_{Lo} \underline{E}_{Trans}^* + \underline{E}_{Trans} \underline{E}_{Lo}^* \right\} \quad (A-7)$$

re

$$\underline{E}_{Lo} \underline{E}_{Lo}^* = |\underline{U}_2|^2$$

(A-8)

$$\underline{E}_{Trans} \underline{E}_{Trans}^* = \mu^2 L^2(\vec{p}, t) |\underline{U}_1|^2 e^{2X(\vec{p}, t)} + \mu^2 |\underline{E}_N(\vec{p}, t)|^2 + 2\mu^2 L_1(\vec{p}, t) \underline{U}_1 \cdot \underline{E}_N(\vec{p}, t) e^{X(\vec{p}, t)} \cos[\theta_N(\vec{p}, t) - \phi(\vec{p}, t) - \psi(\vec{p}, t)] \quad (A-9)$$

$$\underline{E}_{Lo} \underline{E}_{Trans}^* + \underline{E}_{Trans} \underline{E}_{Lo}^* = 2\mu L(\vec{p}, t) |\underline{U}_1| |\underline{U}_2| e^{X(\vec{p}, t)} \cos[\vec{p}_p \cdot \vec{p} - \phi(\vec{p}, t) - \psi(\vec{p}, t)]$$

$$+ 2\mu \underline{E}_N(\vec{p}, t) \underline{U}_2 \cos[\vec{p}_p \cdot \vec{p} - \theta_N(\vec{p}, t)] \quad (A-10)$$

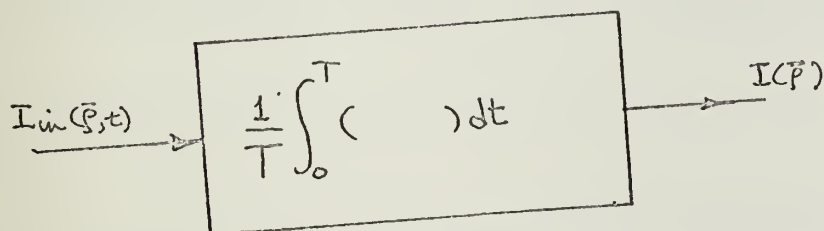


FIGURE A-1

BLACK BOX MODEL OF DETECTOR

Due to the shortness of the shutter period compared to the atmospheric processes, all the terms except those containing noise factors are constant over the sample period T. Only the noise terms will vary; thus the integrating effect of the detector will act only on the terms

$$\mu^2 \left| E_n(\bar{\rho}, t) \right|^2$$

$$2L(\bar{\rho}, t) \mu^2 \underline{U}_1 E_n(\bar{\rho}, t) e^{X(\bar{\rho}, t)} \cos[\Theta_n(\bar{\rho}, t) - \phi(\bar{\rho}, t) - \psi(\bar{\rho}, t)]$$

and $2\mu \underline{U}_2 E_n(\bar{\rho}, t) \cos[\bar{\beta}_\rho \cdot \bar{\rho} - \Theta_n(\bar{\rho}, t)]$

The integral of the first term, the square of the envelope of a complex Gaussian process, is a relatively long-term integration of a very wide bandwidth process; thus the time integration can be replaced with the ensemble average

$$\frac{1}{T} \int_0^T \mu^2 |E_n(\bar{\rho}, t)|^2 dt = E[\mu^2 |E_n(\bar{\rho}, t)|^2] = N^2$$

where N^2 is proportional to the average power in the relevant background radiation.

Similarly, the time integrals of the terms containing both $E_n(\bar{\rho}, t)$ and $\Theta_n(\bar{\rho}, t)$ may be replaced with ensemble averages since both $E_n(\bar{\rho}, t)$ and $\Theta_n(\bar{\rho}, t)$ are very wide bandwidth processes compared to the integration time T . Thus, for example

$$\frac{1}{T} \int_0^T 2\mu \underline{U}_2 E_n(\bar{\rho}, t) \cos[\bar{\beta}_\rho \cdot \bar{\rho} - \Theta_n(\bar{\rho}, t)] dt = E[2\mu \underline{U}_2 E_n(\bar{\rho}, t) \cos[\bar{\beta}_\rho \cdot \bar{\rho} - \Theta_n(\bar{\rho}, t)]]$$

Further, the two processes $E_n(\bar{\rho}, t)$ and $\Theta_n(\bar{\rho}, t)$ are independent, so that

$$E[2\mu \underline{U}_2 E_n(\bar{\rho}, t) \cos[\bar{\beta}_\rho \cdot \bar{\rho} - \Theta_n(\bar{\rho}, t)]] = E[2\mu \underline{U}_2 E_n(\bar{\rho}, t)] E[\cos[\bar{\beta}_\rho \cdot \bar{\rho} - \Theta_n(\bar{\rho}, t)]]$$

Also, $\Theta_n(\bar{\rho}, t)$ is reasonably modeled as approximately uniformly distributed between 0 and 2π at any time during the period 0 to T . Thus $E[\cos[\bar{\beta}_\rho \cdot \bar{\rho} - \Theta_n(\bar{\rho}, t)]]$ tends towards zero and the time integral is approximately zero over the entire surface. Similarly, the

$$2L(\bar{\rho}, t) \mu^2 \underline{U}_1 E_n(\bar{\rho}, t) e^{X(\bar{\rho}, t)} \cos[\Theta_n(\bar{\rho}, t) - \phi(\bar{\rho}, t) - \psi(\bar{\rho}, t)]$$

term tends towards zero.

This integration model of the detector implies that the detector records energy. For this model, since the processes are slow compared to the shutter time, a typical intensity, $I(\bar{\rho})$, has been used with the understanding that multiplication by T , the integration time constant, will yield the proper energy terms.

The resulting output from this integration model is thus

$$I(\bar{\rho}) = \frac{1}{2\eta} \left\{ \left| \underline{U}_2 \right|^2 + \mu^2 L(\bar{\rho}) \left| \underline{U}_1 \right|^2 e^{2X(\bar{\rho})} + N^2 + 2\mu L(\bar{\rho}) \left| \underline{U}_1 \right| \left| \underline{U}_2 \right| e^{X(\bar{\rho})} \cos[\bar{B}_\rho \cdot \bar{\rho} - \phi(\bar{\rho}) - \psi(\rho)] \right\} \quad (\Lambda-11)$$

The loss term $L(\bar{\rho})$ is reasonably modeled as a uniform quantity over the strong portion of the transmitted beam since scattering and molecular absorption are essentially non-preferential and are less apparent in the strong portion of the beam. As it is this portion of the beam that will be collected, the term $L(\bar{\rho})$ will be replaced with L .

The term $\psi(\bar{\rho})$ represents the phase modulation due to mirror vibrations further acted on by the turbulent channel. Due to mirror mount massiveness, the value of $\psi(\bar{\rho}, t)$ is constant with time over the shuttering period. The spatial variation of $\psi(\bar{\rho})$ is critical, however, since the mirror movements that can occur cause a tilt on the reflected wave. This tilt is of the same form that one expects as the first order effect of atmosphere distortion.

There are arguments that seem to indicate that while this tilt caused by the mirror is a limitation on the system, the mea-

surements of the atmospheric effects can still be made. The first is that typical tilt changes between photographs are on the order of 15 microradians. If this tilt change were due only to mirror movements, this would mean a beam movement of 0.05 inch at the telescope. The overlap of the returned beam over the receiving was approximately 0.5 inches, meaning that this movement could not be seen. However, more significant tilt changes would be 100 plus microradians, which translates to a 0.5 inch travel at the telescope. Thus this movement would be seen and neglected. Thus it is recognized that mirror motions are critical, but for this path do not swamp out larger values of atmospheric tilt. Therefore, $\psi(\bar{\rho})$ will be lumped in $\phi(\bar{\rho})$, and the intensity can be written as

$$I(\bar{\rho}) = \frac{1}{2\eta} \left\{ \left| U_2 \right|^2 + N^2 + \mu^2 L^2 \left| U_1 \right|^2 e^{2X(\bar{\rho})} + 2\mu L \left| U_1 \right| \left| U_2 \right| e^{X(\bar{\rho})} \cos[\bar{\theta}_\rho \cdot \bar{\rho} - \phi(\bar{\rho}) - \alpha] \right\} \quad (\text{A-12})$$

where the intensity contains a term phase modulated by the atmospheric phase distortion.

A - 2 Electronics

The data analysis system was built around the Packard Bell 920 television camera and is shown in block diagram form in Fig. A-2. As produced, the camera has a 2:1 random interlace which was altered to a single vertical scan to allow accurate reading of the fringe pattern. The sweep of the television camera was made into 256 horizontal lines each vertical sweep, with synchronization between the horizontal and vertical rasters. The circuits used for this system were built around RTL digital integrated-circuits.

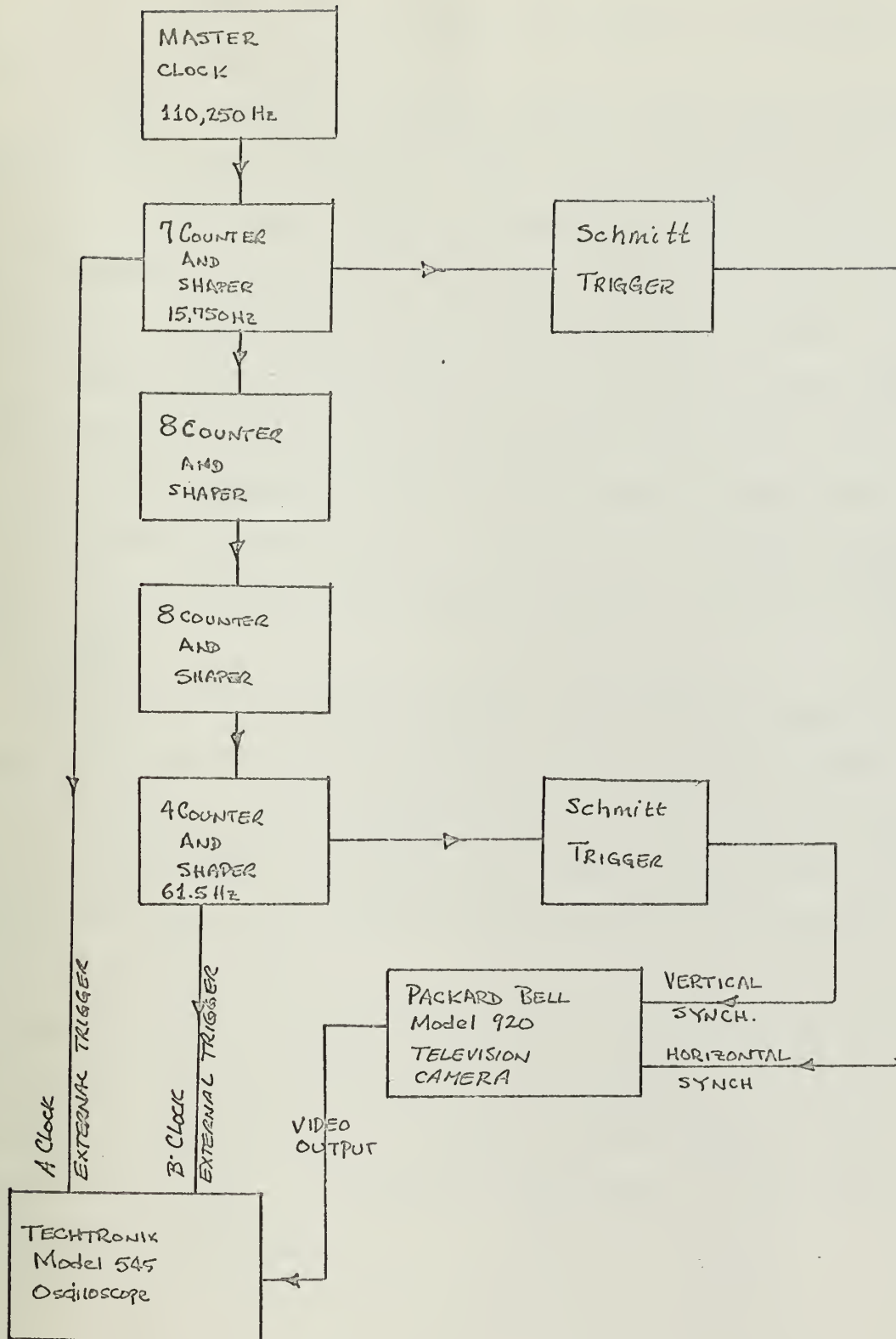


Figure A-2 Data Analysis System Block Diagram

A master clock shown in Fig. A-3 was used to generate the pulse train for the system.

A series of counters and pulse shapers were used to generate synchronization pulse trains from the master clock signal. In each case a synchronous counter was used to minimize countdown delays inherent in sequential counters. Figs. A-4, A-5 and A-6 are circuit diagrams for these counters and pulse shapers. In each of the circuits the counting is done by the JK flip-flops gated on and off by the logic. The shapers were pulse generators with a variable resistor used to set the output pulse width.

The synchronization pulses were put into Schmitt trigger circuits to provide some power gain and also to buffer the counter circuits.

Using the system outlined above, the television camera scan was made to cover the 256 horizontal lines in each vertical sweep with no interlace. The starting point for each vertical sweep was the same so that the video output could be displayed on an oscilloscope, using the synchronization pulses as triggers, with precision and stability.

Before display, the video output of the television camera was put into a low pass filter with a 3 db point at 4 MHz. The low pass filtering was done to remove a large amount of high frequency hash. Fig. A-7 shows the improvement of the display produced by this filtering.

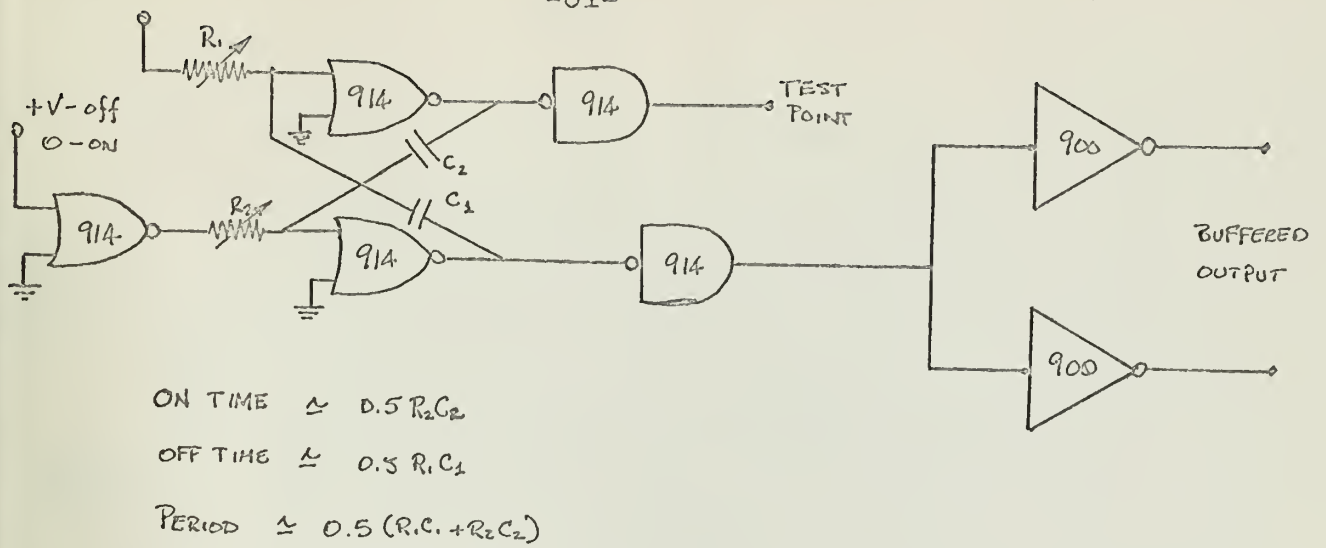


Figure A-3 Master Clock and Pulse Generator for Synchronization System

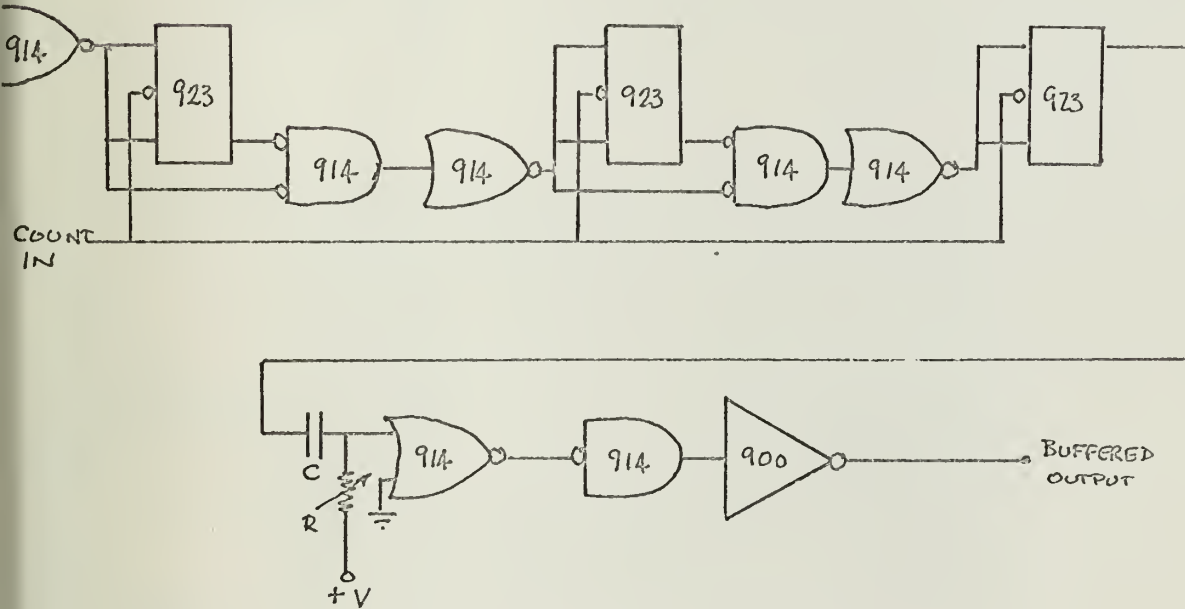


Figure A-4 Eight Counter and Pulse Generator

Figure A-5 Seven Counter and Pulse Generator

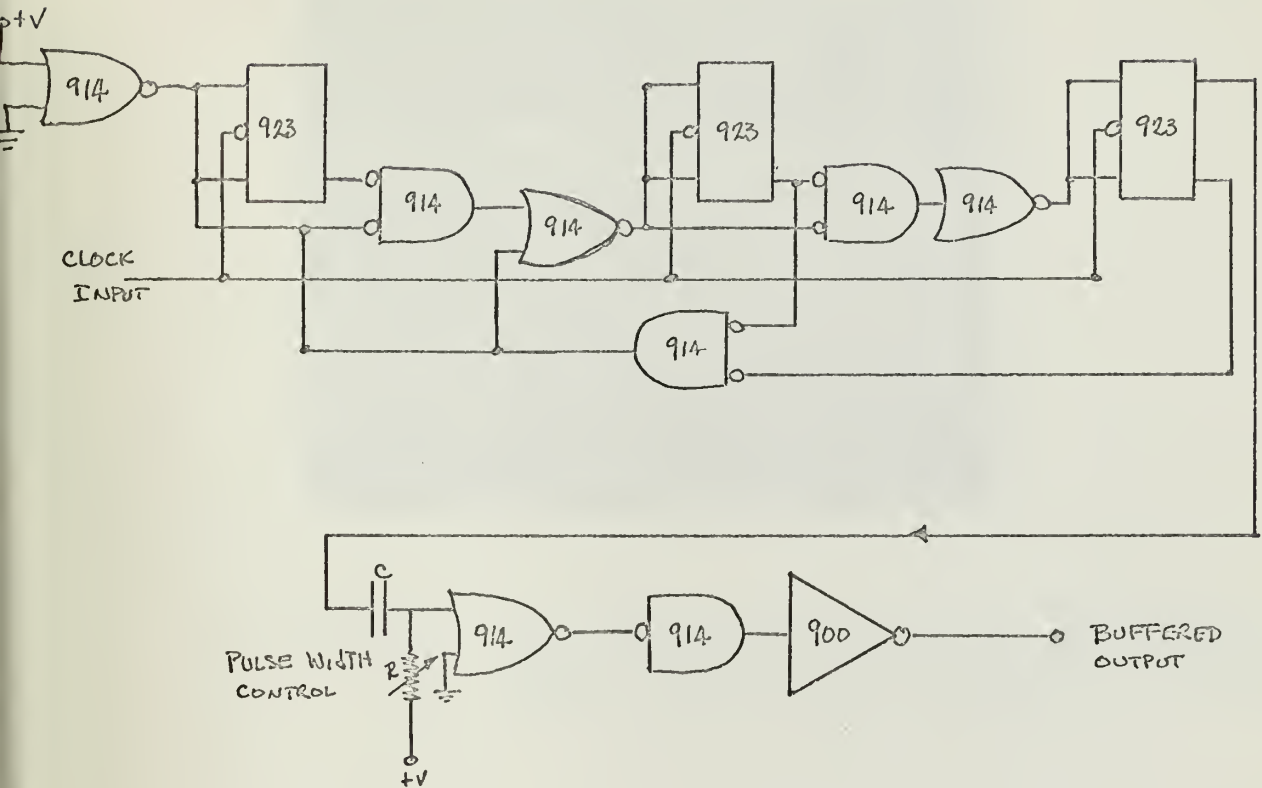


Figure A-6 Four Counter and Pulse Generator

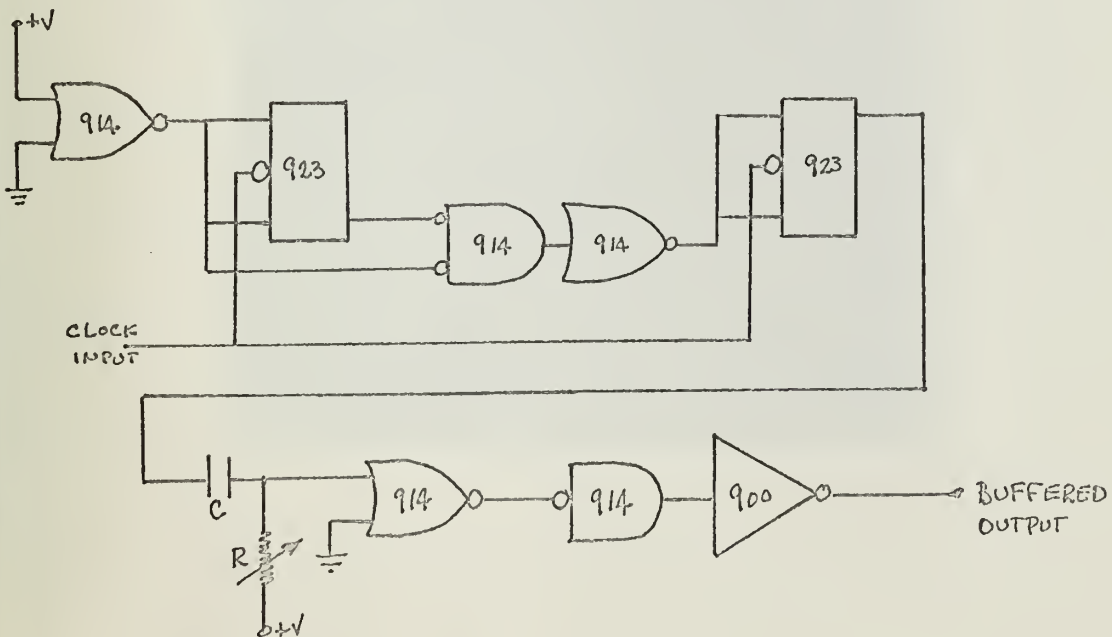




Figure A-7. Improvement in Picture Quality from Insertion of Low Pass Filter at the Television Video Output. Upper Picture is without filtering; Lower Picture is with filtering.



APPENDIX B

This appendix contains a discussion of the data analysis system limitations.

B - 1 Fringe Pattern Model

As shown in Appendix A, the intensity for plane wave models is

$$I(\bar{\rho}) = \frac{1}{2\eta} \left\{ \left| \underline{U}_2 \right|^2 + N^2 + \frac{2}{X(\bar{\rho})} \left| \underline{U}_1 \right|^2 e^{2x(\bar{\rho})} + 2\mu L \left| \underline{U}_1 \right| \left| \underline{U}_2 \right| e^{\cos[\bar{\beta}_\rho \cdot \bar{\rho} - \phi(\bar{\rho}) - \alpha]} \right\} \quad (A-12)$$

The fringes result from the spatial sinusoid, which is proportional to the product of the two signals. The fringes ride a bias which is the sum of the intensities of the two signals. The terms representing atmospheric turbulence effects can be thought of as minified representations of the processes at the objective of the receiving telescope. Thus

$$X(\bar{\rho}) = X(\bar{\rho}'/\mu)$$

$$\phi(\bar{\rho}) = \phi(\bar{\rho}'/\mu)$$

where

$\bar{\rho}$ is the two dimensional vector at the detector surface

$\bar{\rho}'$ is the two dimensional vector at the objective plane oriented so that the geometry, when propagated through the receiver optics, matches that of $\bar{\rho}$.

μ represents the magnification of the telescope-eyepiece combination

Further, aligning the geometry of this model so that the fringe lines coincide with one of the axes in the $\bar{\rho}$ plane simplifies the notation. With this assumption, the intensity is

$$I(\bar{\rho}) = \frac{1}{2\eta} \left\{ \left| \underline{U}_1 \right|^2 + N^2 + \mu^2 L^2 \left| \underline{U}_2 \right|^2 e^{2X(\bar{\rho})} \right. \\ \left. + 2\mu L \left| \underline{U}_1 \right| \left| \underline{U}_2 \right| \cos[\beta_x x - \phi(\bar{\rho}) - \alpha] \right\}$$

where

$$\beta_x = |\beta| (\beta_x / |\beta|) = |\beta| \sin \ell = \frac{2\pi}{\lambda} \sin \ell \approx 2\pi \ell / \lambda$$

ℓ represents the angle between the two interfering waves and is set by the experimenter so that $\ell \ll 1$

By looking at a very narrow strip in the y dimension so that variations in y do not have a chance to occur, the intensity model can be written as

$$I(\rho) = \frac{1}{2\eta} \left\{ \left| \underline{U}_1 \right|^2 + N^2 + \mu^2 L^2 \left| \underline{U}_2 \right|^2 e^{2X(x, y_0)} \right. \\ \left. + 2\mu L \left| \underline{U}_1 \right| \left| \underline{U}_2 \right| e^{X(x, y_0)} \cos\left[\frac{2\pi \ell x}{\lambda} - \phi(x, y_0) - \alpha\right] \right\} \quad (B-1)$$

The problem of seeing the fringe pattern is related to the depth of modulation, which can be shown in this model to depend on the visibility ratio V, defined as

$$V = \frac{\text{amplitude of sinusoid}}{\text{amplitude of bias}} \\ = \frac{2\mu L \left| \underline{U}_1 \right| \left| \underline{U}_2 \right| e^{X(\bar{\rho})}}{\left| \underline{U}_2 \right|^2 + N^2 + \mu^2 L^2 \left| \underline{U}_1 \right|^2 e^{2X(\rho)}} \quad (B-2)$$

For this experiment, N was negligible compared to the other terms in the denominator and will be neglected. The other terms in the denominator represent the local oscillator and received beam intensities. The shadow pattern of these intensities can be seen during experimentation. From observation, the shadow pattern of the received field is brighter than the local oscillator by an estimated factor of three to four. On a longer path, losses will surely be more severe and this ratio would be reversed. If Eq. B-2

is manipulated slightly, and the information on the ratio of the two beam intensities incorporated, the visibility ratio becomes

$$V = \frac{2 (\mu L |\underline{U}_1| / |\underline{U}_2|) e^{X(\bar{\rho})}}{1 + \frac{\mu^2 L^2 |\underline{U}_1|^2}{|\underline{U}_2|^2} e^{2X(\bar{\rho})}}$$

$$= 2 \frac{K e^{X(\bar{\rho})}}{1 + K^2 e^{2X(\bar{\rho})}} = \frac{4 e^{X(\bar{\rho})}}{1 + 4 e^{2X(\bar{\rho})}} \quad (B-3)$$

It can be seen that the scintillation process is the fundamental limitation on modulation depth for this path. This is plotted in Fig. B-1.

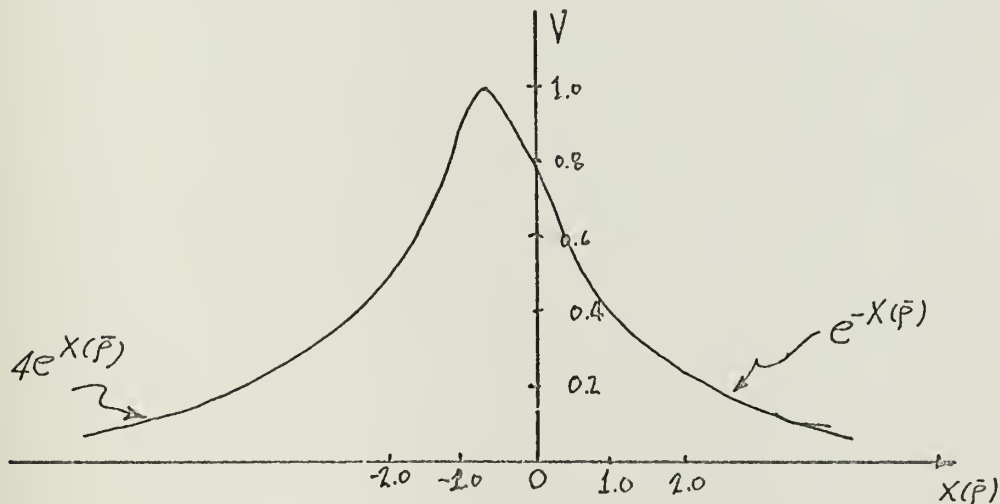


Figure B-1 Plot of Visibility Ratio with changes in the value of scintillation

A further limitation peculiar to this particular data analysis system was the resolution available using an oscilloscope display for detailed analysis. The scope face was ten centimeters across and distinctive portions of the waveform could be located accurately to one-half millimeter as long as

the surrounding clutter was not too bad. However, at least a three to five millimeter separation was required before it was possible to reliably distinguish peaks from clutter for the typical depths of modulation produced by the scanned fringe lines. This means that 20 to 33 lines maximum could be handled on the scope. It was found that (see section 3-1) the effects of the atmospheric turbulence on the fringe perturbations did not become easily visible until the number of fringes across the aperture became twenty or less. Thus the use of the scope was not a serious limitation for this experiment.

BIBLIOGRAPHY

1. Tatarski, V. I., Wave Propagation in a Turbulent Medium, McGraw-Hill Book Co., New York, 1961.
2. Hufnagel, R. E., and N. Stanley, "Modulation Transfer Function Associated with Image Transmission through Turbulent Media", J. Opt Soc. Am., Vol. 54, No. 1, January 1964. pp. 52-61.
3. Beckman, P., "Signal Degeneration in Laser Beams Propagated Through a Turbulent Atmosphere", Radio Science J. of Research, NBS/USNC-URSI, Vol. 69D, No. 4, April 1965.
4. Goldstein, I., Miles, P. A., and Chabot, A., "Heterodyne Measurements of Light Propagation through Atmospheric Turbulence", Proc. of IEEE, Vol. 53, No. 9, September 1965, pp. 1172-1180.
5. Fried, D. L., "Statistics of a Geometric Representation of Wavefront Distortion", J. Opt. Soc. Am., Vol. 55, No. 11, Nov. 1965, pp. 1427-1435.
6. Subramanian, M. and J. A. Collinson, "Modulation of Laser Beams by Atmospheric Turbulence", Bell System Technical Journal, Vol. 44, March 1965, pp. 543-546.
7. Hogg, D. C., "On the Spectrum of Optical Waves Propagated Through the Atmosphere", Bell System Technical Journal, Vol. 42, November 1963, pp. 2967-2969.
8. Goodwin, F. E., "The Measurement of Optical Phase Noise Over Long Atmospheric Paths", Hughes Research Labs., Malibu, Calif. (Presented at the "Boulder Conference on Atmospheric Limitations to Optical Propagation", March 1965).
9. Hoversten, E. V., "The Atmosphere as an Optical Communication Channel", IEEE International Convention Record, Vol. 15, Part II, March 1967, pp. 137-145.

ACCOPRESS®

CLOTH BOUND BINDER

BF 2507	RED	BS 2507	TURQUOISE
BG 2507	BLACK	BQ 2507	PALM GREEN
BD 2507	GREY	BX 2507	EXECUTIVE RED
BP 2507	GREEN	BZ 2507	DARK GREEN
BU 2507	BLUE	BA 2507	TANGERINE
BY 2507	YELLOW	BB 2507	ROYAL BLUE
2507	CB-D50		ASSORTED DISPLAY

PAT. PENDING

thesT135

Heterodyne measurements of atmospheric p



3 2768 001 01374 1

DUDLEY KNOX LIBRARY